Preprint Cambridge Centre for Computational Chemical Engineering ISSN 1473 – 4273

Influence of the types of oxygenated fuels on the characteristics of soot emitted from a CI engine

Yong Ren Tan[1,2,3], Qiren Zhu[2,3], Yichen Zong[2,3], Jiawei Lai[4], Maurin Salamanca[5], Jethro Akroyd[1,2,4], Wenming Yang[2,3], Markus Kraft[1,2,6,7]

released: October 26, 2022

[1] Department of Chemical Engineering
and Biotechnology
University of Cambridge
Philippa Fawcett Drive
Cambridge, CB3 0AS
United Kingdom

[2] CARES
Cambridge Centre for Advanced
Research and Education in Singapore
1 Create Way
CREATE Tower, #05-05
Singapore, 138602

[3] Department of Mechanical Engineering
National University of Singapore
9 Engineering Drive 1
Singapore, 117576

[4] CMCL Innovations
Sheraton House
Cambridge
CB3 0AX
United Kingdom

[5] Grupo Ciencia de Materiales Avanzados
Universidad Nacional de
Colombia-Sede Medellín
Carrera 65 A No 59A-110
Medellín, Colombia

[6] School of Chemical
and Biomedical Engineering
Nanyang Technological University
62 Nanyang Drive
Singapore, 637459

[7] The Alan Turing Institute
London
United Kingdom

Preprint No. 298

Keywords: Polyoxymethylene dimethyl ether, Particle size distribution, Particulate matter, Soot, CI engine

Edited by
Computational Modelling Group
Department of Chemical Engineering and Biotechnology
University of Cambridge
Philippa Fawcett Drive
Cambridge, CB3 0AS
United Kingdom

E-Mail: mk306@cam.ac.uk
World Wide Web: https://como.ceb.cam.ac.uk/

Abstract

Dimethyl carbonate (DMC), ethanol (EtOH), polyoxymethylene dimethyl ether 1 (PODE1) and polyoxymethylene dimethyl ether 4 (PODE4) were blended with Jet A1 into fuel mixes with 5% oxygen content to investigate the effect of the oxygenated fuels on the soot produced from a compression ignition engine. Particle size distribution (PSD) was measured using a differential mobility spectrometer. Thermogravimetric analysis (TGA), Raman spectroscopy, ultraviolet-visible spectroscopy (UV-Vis) and Fourier transform infrared (FT-IR) spectroscopy were performed on the soot collected. PSD measurements showed that the addition of EtOH promoted the formation of nucleation mode particles. Based on measurements from Raman spectroscopy, the soot from oxygenated fuel blends is more disordered than Jet A1. Meanwhile, TGA showed that the soot from oxygenated fuel blends oxidises at a lower temperature than Jet A1. The lowered oxidation temperature of soot from oxygenated fuel blends coincides with the presence of a higher proportion of oxygen functional groups in FT-IR spectra for oxygenated fuel soot samples. Lastly, the conjugation length of the soot aromatic structure for the organic carbons (derived from the optical band gap of UV-Vis) is greater for the oxygenated fuel blends, indicating that the growth of organic carbons is enhanced for oxygenated fuel blends. The blending of oxygenated fuels influences soot properties through the dilution effect, combustion condition effect and chemical effect. Particularly, the type and characteristics of oxygenated species from the decomposition of the oxygenated fuels during combustion can considerably affect the soot properties during combustion.

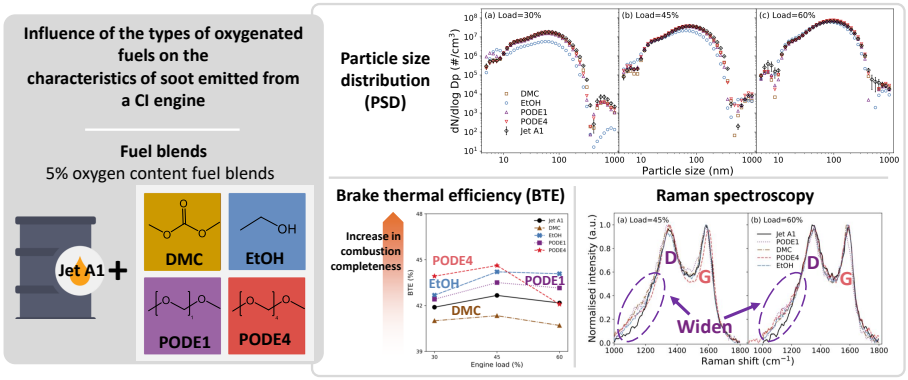

Highlights

- Blending PODE4 in Jet A1 can increase CI engine BTE by up to 4.8% at engine load 30%
- Soot samples from oxygenated fuels especially PODE1 are more reactive and disordered
- Chemical properties of oxygenated fuels are vital in affecting soot characteristics

Contents

1 Introduction

Clean electrification is essential to meeting the clean energy transition by 2050 [28]. Nevertheless, even in the ideal Net Zero Emission 2050 scenario, electricity will only comprise less than half of the total energy consumption in 2050 [28]. The combustion of fuels from various sources will remain significant in the global energy mix [28].

The combustion of fossil fuels releases carbon dioxide, methane, soot, ultrafine particles ($PM_{0.1}$), and other pollutants into the atmosphere, which contributes to climate change [9, 35]. Alarmingly, air pollution was responsible for 6.7 million deaths globally in 2019 [22]. Moreover, human exposure to pollutants (especially soot [29, 47, 61] and $PM_{0.1}$ [16, 19]) released from the combustion of fuels can have adverse health implications. Consequently, fuels that can be combusted cleanly and sourced sustainably with a low carbon footprint are imperative to meeting our climate goals [28] and improving global health [22]. Notably, the usage of sustainable aviation fuels has shown to reduce the emission of particulates and the overall carbon footprint [62].

The incorporation of sustainable, low emissions alternative fuels into the global energy mix is indispensable in the heavy transport and aviation sectors where electrification is challenging [25]. These sectors are expected to be the main consumers of alternative fuels by 2050 [28]. The combined global total emissions from heavy transportation and aviation are expected to grow to 32% by 2050 (currently at 11%) [45]. With support from governmental policies, the demand for alternative fuels is expected to reach 3.5 mboe/d[1] (from 2 mb/d[2] in 2020) by 2030 [28] with a market value of *ca.*USD 40–50 billion [25].

Given the increasing importance of alternative fuels in combustion, there is a need to examine and evaluate their impact on the environment and human health. They are typically sourced from sustainable resources such as biomass. As they often contain oxygen within their chemical structures, they are also known as oxygenated fuels [32]. Hence they differ in the type and composition of combustion products from their fossil-based counterparts when combusted. Most often, oxygenated fuels can readily be blended with fossil fuels to reduce overall emissions, without requiring expensive changes to existing internal combustion engines, vehicle fuel systems, or fuel distribution networks [25].

Some common oxygenated fuels blended with fossil fuels that have been studied in engine systems are alcohols, polyoxymethylene dimethyl ethers (PODEn or also known as OME) and carbonate ester [1, 23, 27, 40]. Generally, the increase in the blending of the oxygenated fuels decreases the particulate emission from the engine. Ethanol (EtOH) is one of the most prominent alcohols that have been used commercially [49]. The blending of 10–15 vol.% of EtOH with diesel can significantly reduce particulate emission on about two-thirds of engine maps [23, 27]. Meanwhile, PODEn has promising potential for clean combustion, often attributed to its high oxygen content and lack of carbon-carbon bonds in its molecular structure [40]. The blending of 10% PODE3 in diesel showed up to a 60% reduction in soot formation when combusted in a compression ignition engine, attributed to the enhanced oxidation provided by the addition of PODE3 towards soot reduction [36]. Dimethyl carbonate (DMC) is also an oxygenated fuel that has high oxygen

[1] mboe/d = million barrels of oil equivalent per day

[2] mb/d = million barrels per day

content and can readily be produced from captured CO_2 in the atmosphere [1]. The soot formed from the blending of DMC with diesel has shown a reduction in the diameter of the primary particles by 37% [81].

There is also a growing interest to investigate and compare the differences in the molecular structure of the oxygenated fuels with the same oxygen content of fuel blends. For example, the carbon-carbon chain length effect has been studied for alcohols [79]. In the study, methanol, *n*-butanol and *n*-octanol were blended with diesel at 5% oxygen content to study the graphitisation degree of the soot. The soot graphitisation degree was higher when alcohols were added to the diesel, *i.e.* the soot graphitisation increased with the increase in the carbon-carbon chain length of the alcohols [79].

Other than the carbon-carbon chain length effect, the types of the oxygenated fuel functional groups can impact the characteristics of the soot formed. Fundamental studies under lab-scale flames showed that the type of the functional group of the oxygenated fuel influences the soot formed because of the different decomposition pathways of each oxygenated fuels [69–72]. In engine experiments, when the blending of Eucalyptus oil (ether), tea tree oil (alcohol) and biodiesel (methyl ester) were kept at 2.2% oxygen content in diesel, the primary particle diameter decreased by 25.5%, 22.6% and 4.5% respectively [76].

Another investigation using a single engine load, with the blending of methanol, PODE1 and DMC in diesel at 5% oxygen content has shown a reduction in the primary particle size of the soot particles at 13%, 12% and 5% in comparison to the case for diesel [82]. The particles with the oxygenated fuels also have less compactly-clustered morphologies than diesel particles [82]. A follow-up investigation also revealed that the soot from the methanol fuel blend has the most disordered nanostructure, followed by diesel, PODE1 and DMC [83]. This has shown that there is still room for improvement in the investigation of the trends in the soot characteristics when different oxygenated fuels are blended with fossil fuels.

The **purpose of this paper** is to expand on the understanding of the soot formed from the combustion of selected oxygenated fuel-Jet A1 blends in a compression ignition engine at three different engine loads (30%, 45% and 60%). Both in-situ and ex-situ techniques were employed to investigate and characterise the emission from the engine. Three types of oxygenated fuels were chosen in the current study – alcohols (EtOH), ethers (PODE1 and PODE4) and carbonate ester (DMC). They were blended with Jet A1 fuel to make up fuel blends with 5% oxygen content. With such a combination of oxygenated fuels and fixed oxygen content, the emission and particulate formation between different oxygen-containing functional groups and ether chain length (through PODE1 and PODE4) can be investigated.

2 Experimental methodology and materials

2.1 Engine and test procedure

A single-cylinder diesel engine (Yanmar Holdings Limited, TF120) is used to investigate the impact of different fuels on the performance and emission of the engine. The experimental setup has been reported in detail previously [36] and is illustrated in **Figure 1**. The difference in the setup as compared to the previous work is the addition of a soot collection line, comprising of an in-line filter holder and a vacuum pump connected to the engine exhaust. This is detailed in **Section 2.4**. The specifications of the engine are listed in **Table 1**. The engine has a Denso common rail high-pressure injection system and a next-cycle control system (NCCS). The details of the full capabilities of the NCCS have been described previously [85]. In brief, it is capable of regulating engine parameters to have a desired and consistent output in each engine cycle [85]. The NCCS will rapidly post-process the collected in-cylinder pressure data to be used in a control loop, giving it enough time to adjust engine control parameters and command actuators in the next combustion cycle.

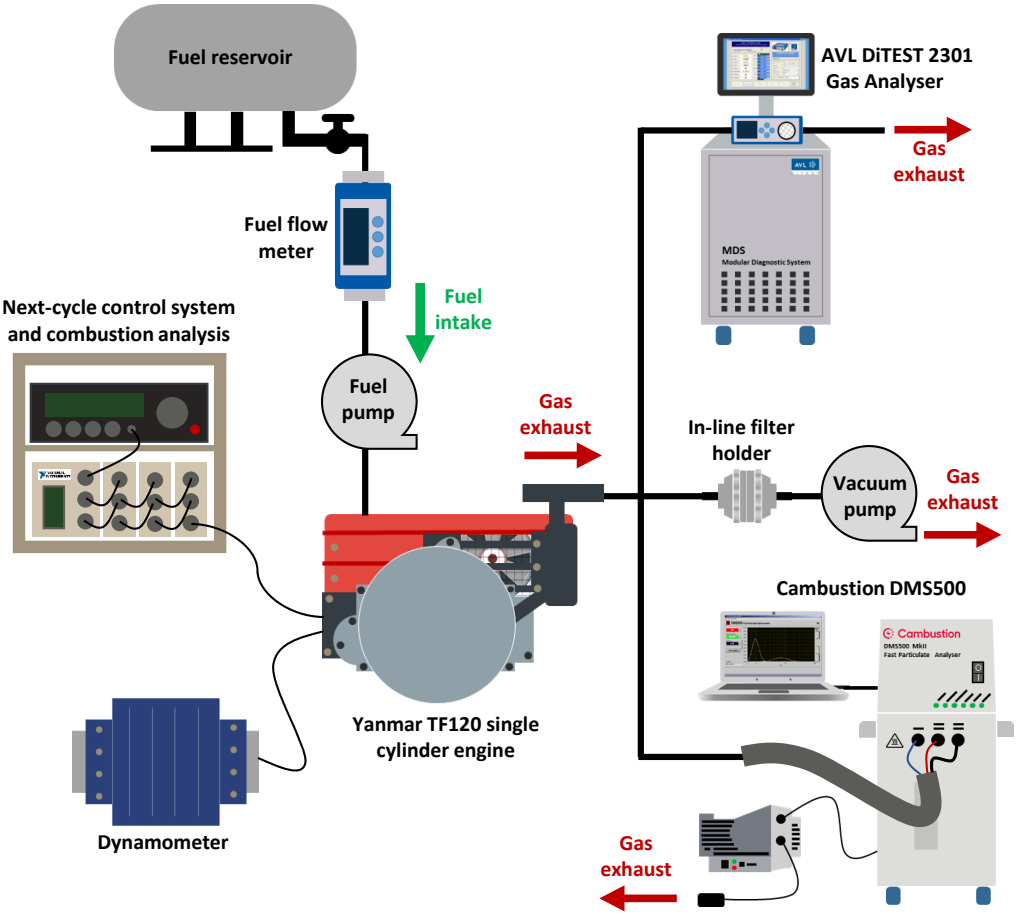

Figure 1: *Schematic diagrams of the experimental setup.*

Table 1: *Characteristics of the engine.*

Type and Configuration	Yanmar TF120
Compression ratio	17.7
Displacement (L)	0.638
Bore/Stroke (mm)	92/96
Maximum torque (Nm)	40 at 1200 rpm

Three engine loads (30%, 45% and 60%) were studied whilst maintaining the engine speed at 1200 rpm. The maximum output torque at 1200 rpm is 40 Nm, giving absolute engine torques of 12, 18 and 24 Nm under the three engine loads, respectively. In each cycle change, the variation in the engine load is within $\pm$ 5%, as measured using a KAMA A.C. synchronous dynamometer (Model ST-7.5). The inlet pressure was maintained at ambient pressure. The same eddy current dynamometer controlled the engine speed and load. The engine start of injection timing was maintained at -20°, 0° ATDC, and the injection pressure was maintained at 40 MPa under all experimental conditions with a double injection strategy. The fuel flow rate was measured using an OVAL Corp. LSN39 flowmeter. The concentrations of CO_2, CO, O_2, NO_x and HC (unburnt hydrocarbon) in the exhaust gas were measured using an AVL DiTEST 2301 gas analyser.

The apparent heat release rate (AHRR) reported in the current investigation is calculated from the in-cylinder pressure data, as detailed in our previous work [36, 85]. The AHRR at any given crank angle degree is given by

$$AHRR = \left[\left(\frac{\gamma}{\gamma-1}\right)P\frac{dV}{dt}\right] + \left[\left(\frac{1}{\gamma-1}\right)V\frac{dP}{dCA}\right], \quad (1)$$

where 'γ' is the ratio of specific heats (assumed to be 1.4), 'P' is the in-cylinder pressure, 'V' is the swept volume, and 'CA' is the crank angle [26]. In the computation of the AHRR, the additional effects from the engine motoring curve have been offset.

2.2 Fuels

Jet A1 fuel is used as the base fuel for all the experimental cases in the current study. The Jet A1 is blended with four different oxygenated fuels to make up to four fuel blends with an oxygen content of 5 mol.%. The four oxygenated fuels used are dimethyl carbonate (DMC), ethanol (EtOH), dimethoxymethane (PODE1) and polyoxymethylene dimethyl ethers 4 (PODE4). The PODE4 was procured from ASG Analytik-Service GmbH with a purity of 98%. DMC, PODE1 and EtOH were procured from Sigma-Aldrich with a purity of at least 99%. The fuels are used without further purification. The composition of the fuel blends tested in this experimental study is detailed in **Table 2**, while some of the important fuel properties are detailed in **Table 3**.

Table 2: *Fuel blend composition and the respective mixture lower heating value.*

Fuel blend	Jet A1 (vol.%)	Oxygenated fuel (vol.%)	Oxygen content (mol.%)	Fuel/fuel blend lower heating value (MJ/kg)
Jet A1	100.0	0.0	0	43.20 [15]
DMC	92.8	7.2	5	40.67 [1, 15]
EtOH	85.4	14.6	5	40.87 [1, 15]
PODE1	88.8	11.2	5	40.77 [15, 39]
PODE4	91.9	8.1	5	40.65 [15, 39]

Table 3: *Fuel properties.*

Fuel properties	Jet A1 [15]	DMC [1]	EtOH [1]	PODE1 [39]	PODE4 [39]
CN	42	35	9	29	90
LHV (MJ/kg)	43.2	15.8	26.7	22.4	18.4
ρ (g/cm^3)	0.82	1.07	0.79	0.86	1.06
υ (mm^2/s)	1.36	0.63	1.37	0.36	1.72

Keys:

CN	Cetane number	LHV	Lower heating value
ρ	Density	υ	Kinematic viscosity

2.3 Particle size distribution

The particle size distribution (PSD) of the electrical mobility diameter and the number concentration of the particulates from the engine exhaust were measured using a DMS500 Differential Mobility Spectrometer from Cambustion Ltd., as reported previously [36, 85]. The range of the electrical mobility diameter of the particulates is 5–1000 nm. The measurement was performed at 10 Hz for three minutes for five repeats. The uncertainty of the measurement is $\pm$ 5%.

2.4 Soot characterisation methods

To analyse the reactivity and other properties such as the nanostructure and the surface functional groups of soot generated from the engine experiments using different oxygenated fuel blends, various materials characterisation techniques are applied. As illustrated in Figure 1, a vacuum pump is used to draw exhaust gas through a Cytiva Whatman^{TM} TE 35 polytetrafluoroethylene membrane filter (0.2 μm pore size, 47 mm diameter), housed in a 47 mm stainless steel in-line filter holder (Pall Corporation, PN 1235). Over a period of time (*ca.*10–15 minutes), the deposited soot on the membrane filter is then abraded using a spatula and collected for further analysis. The soot collection for

engine load of 30% was too low and inefficient for subsequent investigation. Hence, only soot collected from two engine loads (45% and 60%) was used for further study.

2.4.1 Thermogravimetric analysis

Thermogravimetric analysis (TGA) was conducted on a Mettler-Toledo TGA/DSC 2 LF 1100 thermogravimetric analyser. Soot samples of *ca.*3 mg were loaded in an alumina crucible. The program for the TGA is detailed in **Table 4**, based on the program suggested in the literature [54].

Table 4: *Heating program for thermogravimetric analysis (TGA) based on the literature [54].*

Steps	Gas	Gas flow rate (mL/min)	Heating program
1	N_2	10	10 °C/min until 400 °C
2	N_2	10	Isothermal for 60 minutes
3	N_2	10	-20 °C/min until 30 °C
4	Air	10	3 °C/min until 700 °C
5	Air	10	Isothermal for 60 minutes
6	Air	10	-20 °C/min until 30 °C

From the TGA weight change curve, two characteristic temperatures can be obtained to investigate the thermal behaviour of the soot samples: the starting oxidation temperature (SOT) and maximum weight loss rate temperatures ($WLRT_{max}$). The SOT is defined as the temperature when the weight of the soot sample reaches 5% of the initial weight of the sample; while the $WLRT_{max}$ is defined as the temperature corresponding to the maximum weight loss rate [2, 54]. They are reasonably good indicators of the oxidation reactivity of the soot [2, 54]. Furthermore, the oxidation of soot under air can be modelled kinetically through an Arrhenius-type reaction, given by [2, 54],

$$\left(\frac{1}{1-X}\right)\frac{dX}{dt} = k_o \exp\left(-\frac{E_a}{RT}\right), \quad \text{where } X = \frac{m_o - m}{m_o}. \tag{2}$$

'X' is the sample conversion at any time. m_o and m are the initial sample mass (mg) and the carbon mass at a certain time, t, respectively. R (kJ mol^{-1} K^{-1}) is the ideal gas constant. E_a (kJ mol^{-1}) is the activation energy. k_o (s^{-1}) is the pre-exponential factor. T (K) is the reaction temperature. After performing logarithms of **Equation 2** and plotting a graph of $\ln\left[\left(\frac{1}{1-X}\right)\frac{dX}{dt}\right]$ versus $1/T$, a straight line can be obtained. From the gradient of the straight line, the E_a can be computed, which will be used in the current study to compare further the oxidation behaviour of soot from different oxygenated fuel blends.

2.4.2 Ultraviolet–visible spectroscopy

The Ultraviolet–visible (UV-Vis) absorption spectra of the soot samples were measured on a Cary 60 UV-Vis spectrophotometer from Agilent Technologies Inc. Soot sample was

ultrasonically suspended for 15 minutes at room temperature in 1-Methyl-2-pyrrolidone (VWR International LLC, ≥99.5% purity) to make up a soot solution with soot concentration of 10 mg/L. The wavelength range of the UV-Vis spectra measurement was 190–1100 nm with a standard 1 cm path-length quartz cell. The UV-Vis measurement of soot is based on the procedure in the literature [8, 38, 55, 56]. The UV-Vis absorption spectra of the soot samples were analysed using the Tauc method [73] where the optical band gaps of the soot and organic carbon were obtained through their individual contribution to the UV-Vis absorption spectra using the methodology from the literature [57].

2.4.3 Raman spectroscopy

A Horiba Jobin Yvon Modular Raman Spectrometer (514 nm Stellar Pro Argon-ion laser) with 600 lines/mm grating was used to collect of the Raman spectrum of soot samples. The system was calibrated using a silicon reference before the measurement (520.5 cm^{-1}). An OLYMPUS ×50 objective aperture and incident laser power of 20 mW was used to capture the Raman spectra of the soot. All spectra were obtained in extended scan mode in the range of 3500–500 cm^{-1} with 10 seconds per exposure. Raman spectra were recorded at three different positions for each sample. OriginPro (OriginLab Corporation, Version 2021 `9.8.0.200`) was applied to do curving fitting for the spectra, using a 3L1G fitting method, following the recommendations in the literature [67].

Table 5: *Typical Raman shift assignments for soot sample.*

Peak type	Raman shift (cm^{-1})	Name of band	Representation
Lorentzian	1590	G band	Graphite structure
Lorentzian	1350	D1 band	Disordered graphitic lattice
Lorentzian	1200	D3 band	Amorphous carbon
Gaussian	1500	D4 band	Carbon-carbon stretched bonds

2.4.4 Fourier transform infrared spectroscopy

A Fourier transform infrared (FT-IR) spectrometer (Bruker VERTEX 80 FT-IR), fitted with a diffusion reflection accessory (PIKE Technologies Inc., DiffuseIR™ 350-1624100) was used to measure the DRIFT (Diffused Reflectance Infrared Fourier Transform) spectra of the soot samples. Each spectrum is results from 128 accumulated scans at a resolution of 4 cm^{-1} to increase the signal-to-noise ratio. Reference spectra using dried KBr powder (FT-IR grade, Sigma-Aldrich) were always recorded before spectra of the samples were measured. Samples were always diluted by adding KBr until the soot was 1% of the total mass. The samples were measured under Argon at atmospheric pressure. The assignments of the peaks are based on the literature values reported for soot samples [12, 20, 43, 59].

2.5 Engine simulation

Three kinetic models were established by combining different sub-mechanisms from the literature. The kinetic models were used to compare with the experimental results. It should be noted that the current work does not attempt to propose a new comprehensive model for each oxygenated fuel. Rather, the intention is to use three kinetic models sharing the same core mechanism to analyse the combustion of the mixtures of the oxygenated fuels with Jet A1.

The core mechanism is the Jet A1 fuel mechanism developed previously [74]. The sub-mechanisms for PODE [48], DMC [6] and EtOH [52] were combined with the Jet A1 fuel mechanism, ensuring that all three kinetic models use the same core mechanism. The original mechanisms' rate constants and thermodynamic properties were used without further changes. The kinetic models are available in CHEMKIN format in the Supplementary material, accompanied by their corresponding thermodynamic properties.

The gaseous emission from the engine with different fuels is simulated with the model-based workflow [33, 50]. At the initial stage of the workflow, the in-cylinder pressure and engine-out emissions were calibrated using SRM Engine Suite. Later, further computation of the emission species was performed. The workflow is available from the kinetics software from CMCL Innovations Ltd (Version `2021.2.1`), where it has integrated an advanced statistical toolkit and Model Development Suite (MoDS) to perform parameter estimation, model validation and multi-objective optimisation.

The global sensitivity is computed using High Dimensional Model Representation (HDMR) methodology, as outlined in the literature [50, 64]. Through this methodology, the effect of the input parameters over the whole parameter space is calculated, which in turn allows the study of the interactions between the input parameters. More importantly, the ability to evaluate the sensitivity of a physical system to its inputs is vital during the assessment on the significance of an input in models of a physical system. This is different from the conventional local sensitivity analysis, which calculates the effects of the input parameters about a given point only.

The experimental results of the in-cylinder pressure were modelled using the combined kinetic models from the current investigation with experimental results [85]. After the test simulations, it is confirmed that including the PODE, DMC and EtOH sub-mechanisms does not compromise the capability of the mechanisms to simulate the combustion behaviour of Jet A1 in the engine. Details of the results can be found in the **Section A.1** of the Supplementary material. Additionally, there is a good agreement between the simulated in-cylinder pressure and the experimental in-cylinder pressure for all the cases. Example of all the engine cases for Jet A1 is presented in **Section A.2**. This is crucial because the combustion behaviour, *i.e.* the in-cylinder pressure must be modelled accurately to ensure the reliability of further coupling of different phases of species with the detailed mechanisms. In order to obtain the emission results, the necessary precursors need to be present in the gas phase and this is only possible if the combustion characteristics are captured correctly.

3 Results and discussion

The experimental and simulation results of the current investigation on the combustion of the selected oxygenated fuel blends in a CI engine are presented and discussed in this section. Specifically, three core categories of the results presented are

a) Engine combustion and performance;

b) Engine gaseous emission (supplemented with engine simulation results); and

c) Soot characterisation and analysis.

3.1 Combustion characteristics

Figure 2 shows the in-cylinder pressure for the fuel blends at three engine loads (30%, 45% and 60%). The main trend observed is that fuel blends with oxygenated fuels generally have lower peak in-cylinder pressure as compared to the case for Jet A1. Table 3 shows the lower heating value (LHV) for all the fuel blends studied. Oxygenated fuel blends have slightly lower LHV (by *ca.* 3 MJ/kg) than Jet A1. This results in the oxygenated fuel blends having lower energy density than Jet A1. Therefore, during the combustion in the engine, the oxygenated fuel blends release less heat in the cylinder than Jet A1. This consequently reduces the overall peak in-cylinder pressure in the engine, as observed in the figure.

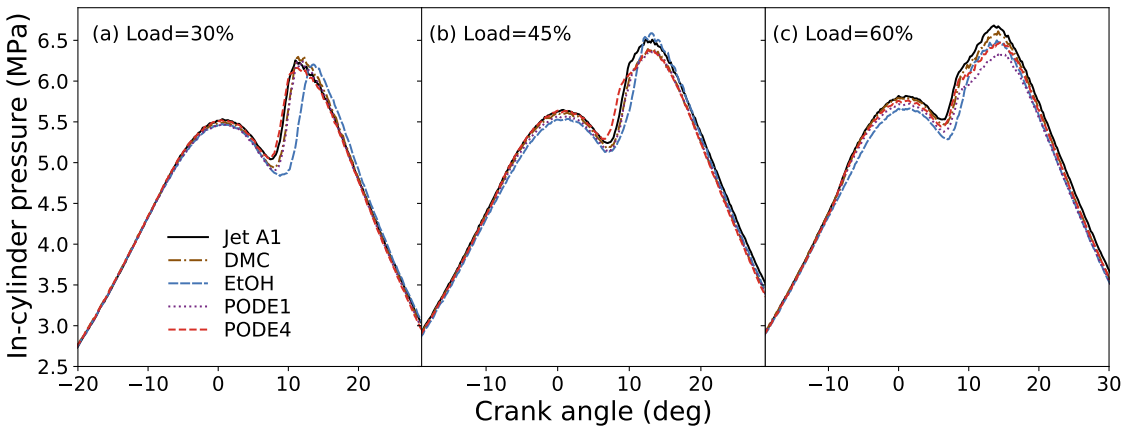

Figure 2: *In-cylinder pressure profiles for the engine with different fuel blends. The data in each panel are grouped by the engine load at (a) 30%, (b) 45% and 60%.*

From Figure 2, it is evident is that the peak in-cylinder pressure is delayed once the oxygenated fuels are added. EtOH has the most noticeable delay in the peak in-cylinder pressure. This is related to the ignition delay, which will be discussed quantitatively towards the end of this section.

Figure 3 shows the heat release rate (HRR) for the fuel blends at three engine loads (30%, 45% and 60%). The current HRR profile generally has two peaks. The first peak

(premixed peak) is associated with the premixed-dominated combustion in the engine; the second peak (diffusion peak) is related to diffusion-dominated combustion [18]. At (low) engine load of 30%, the HRR profile has a strong premixed peak with a shoulder diffusion peak. Upon reaching the (high) engine load of 60%, the premixed peak became weaker; the diffusion peak became stronger and more pronounced. Going from low to high engine load, the peak HRR decreases. This is typical behaviour of the HRR profile for the current injection strategy. It is similar to the previously employed injection strategy [88, 89]. Among the fuel blends studied, the HRR behaviour is quite similar among the blends with oxygenated fuels, except for EtOH.

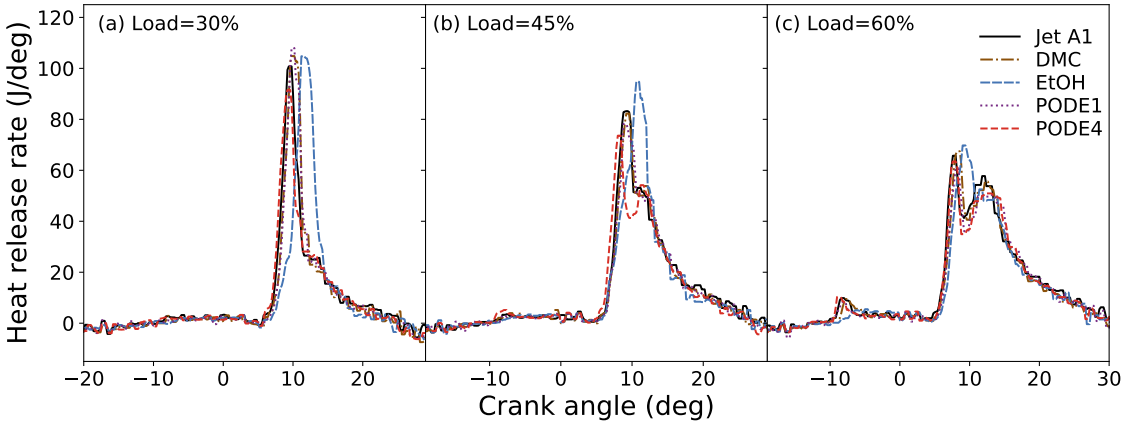

Figure 3: *Heat release rate profiles for the engine with different fuel blends. The data in each panel are grouped by the engine load at (a) 30%, (b) 45% and 60%.*

The HRR profiles of EtOH in all engine loads are distinctively different from the other fuel blends. Uniformly across the three engine loads investigated, its premixed peak is delayed while the diffusion peak remained the same as in the other fuel blends. As a result, the premixed peak appears to merge with the diffusion peak in Figure 3(a) and (b). Additionally, the maximum HRR for EtOH is also the highest among all the cases studied. This suggests that the case for EtOH has an increased amount of premixed combustion and shorter duration of overall combustion compared to the rest of the fuels studied. On the other hand, PODE4 showed a slightly advanced peak HRR and a lower HRR peak compared to Jet A1. These features are related to the higher cetane number (CN) of PODE4, consistent with the work on PODE3 reported previously [36, 37, 88].

Figure 4 shows the ignition delay and the combustion duration for the fuel blends at three engine loads. The ignition delay is defined as the difference in the crank angle (CA) at the start of injection and at the 10% heat release (CA10). It is an indication of the duration of the pre-mixing of the fuel in the engine cylinder before ignition. The combustion duration, meanwhile, is defined as the difference in the CA at the 90% heat release (CA90) and at the 10% heat release (CA10). The data is statistically significant across the fuels and engine load, evident from the two-way analysis of variance (ANOVA) of the ignition delay and the combustion duration, performed at a confidence level of 95% [78]. The ANOVA results are as shown in **Table 9**.

The ignition delay is related to the cetane number (CN) of the oxygenated fuels. Meanwhile, the sensitivity of specific chemical kinetics reactions on the ignition delay (and

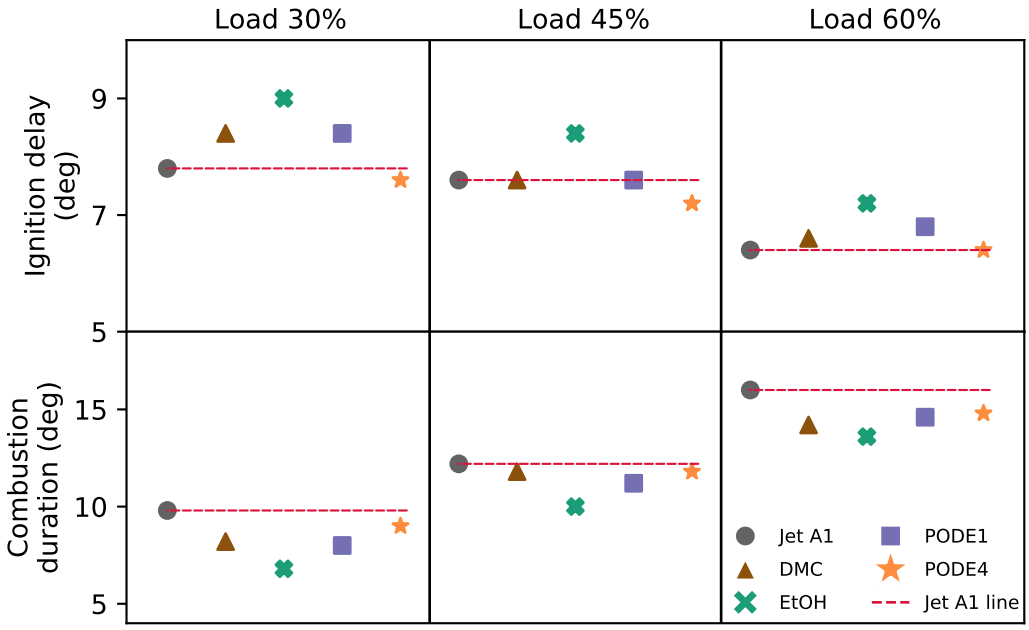

Figure 4: *Ignition delay and the combustion duration for the engine with different fuel blends at engine loads of 30%, 45% and 60%. The read dashed line indicates the measurement for the case of Jet A1 within the subplot for comparison.*

combustion duration) are minimal, as shown in **Section A.3** and in Table 9. As CN is a 'global' property of the combinatory effect of all the chemical kinetics reactions, consideration of the CN in understanding of the behaviour of ignition delay will be the main focus of the discussion.

The ignition delay has a general trend of EtOH $>$ DMC $\approx$ PODE1 $>$ Jet A1 $\geq$ PODE4, which is negatively correlated to the CN of the fuels. Meanwhile, the combustion duration has an opposite trend: EtOH $<$ DMC $\approx$ PODE1 $<$ Jet A1 $\leq$ PODE4. This shows that the EtOH fuel blend has the shortest combustion phasing (most extended ignition delay) and this causes a large amount of heat to be released (highest peak HRR in Figure 3) within a short time frame. The rest of the oxygenated fuel blends have similar ignition delay and combustion duration to Jet A1. Hence, the CI engine may not require modifications to use such oxygenated fuel blends. EtOH, on the contrary, induced a larger change in the ignition and combustion properties, hence the CI engine may need modifications to accommodate the change in the overall combustion properties or the injection timing need further optimisations.

3.2 Engine efficiency

Figure 5 shows the brake thermal efficiency (BTE) for each of the fuel blends at different engine loads. BTE is an indicator of the percentage of the conversion of chemical energy from the fuel into the output power from the engine. From the two-way ANOVA of the BTE at a confidence level of 95% (see Table 9) the data is statistically significant

across the fuels only. The change in the BTE for increased engine load is statistically insignificant. This suggests that within the engine loads studied, the efficiency of the engine to convert the chemical energy from the fuels into output power from the engine is not compromised. Instead, the effect of the blended oxygenated fuels has a significant impact on the BTE.

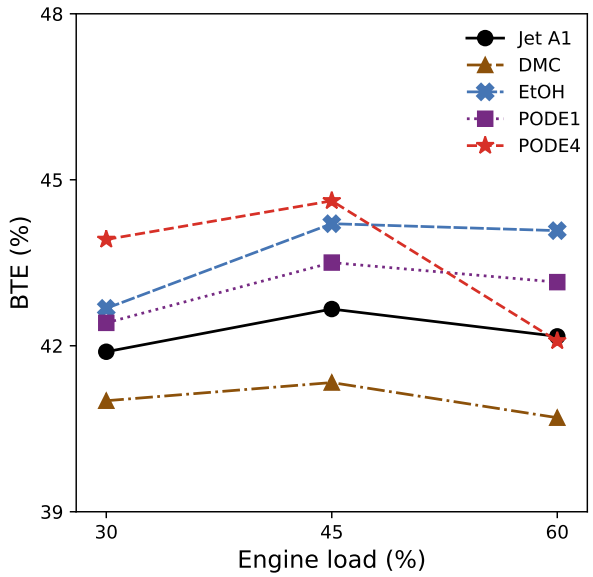

Figure 5: *Brake thermal efficiency (BTE) for the engine with different fuel blends at engine loads of 30%, 45% and 60%.*

PODE4 has higher BTE than Jet A1, up to 4.8%. This can be attributed to the high CN of PODE4 which is double of Jet A1. This improves the combustion speed and performance of the overall fuel blend with Jet A1, hence the high increase in BTE. However, upon reaching a higher engine load of 60%, there is a significant drop in the BTE to the level of Jet A1. This can be due to the change in the combustion mode at engine load 60% (diffusion-dominated combustion) that resulted in the advantage of PODE4 increasing the CN of the fuel blend to be insignificant to improve the BTE.

EtOH and PODE1 have higher BTE (up to 4.5%) than Jet A1. The improvement in BTE for EtOH can be attributed to the enhanced combustion, resulting from the better premixing of the fuels, as reflected in the long ignition delay for EtOH (see Figure 4), leading to more complete combustion. Another possible reason is the hydroxyl group in the molecular structure of EtOH. The breakdown of EtOH forms hydroxyl radical, which can promote oxidation, leading to a more complete combustion [60], contributing to better BTE.

PODE1 has high BTE for a different reason than EtOH due to the difference in physical and chemical properties. The viscosity of PODE1 is much lower than that of Jet A1 (EtOH and Jet A1 have similar viscosity). A lower viscosity can improve the spray atomisation process in the engine, resulting in a more homogeneous mixture of fuel and air for complete combustion, which improves the BTE. Furthermore, the chemical effect of PODE1 can also contribute to the improved BTE as the oxygen radicals and methoxy

radicals are some of the oxygenated species from the decomposition of PODE1 that can promote the oxidation [77]. Notably, the improved BTE of PODE1 is consistent with the results reported in the literature [14, 51].

Intriguingly, PODE4 has a higher BTE than PODE1 at a low engine load. Upon reaching a high engine load, the BTE of PODE1 became higher than PODE4. Despite PODE4 and PODE1 having similar molecular structures apart from the difference in chain length, the viscosity of PODE4 is almost five times larger than PODE1 and the CN of PODE4 is three times larger than PODE1. At a low engine load, with low fuel consumption, the effect of the high CN of PODE4 has contributed to a higher BTE of the engine when compared to PODE1. Upon reaching a high engine load, the fuel consumption increased. The significantly higher viscosity of PODE4 than PODE1 may play a more significant role and consequently, reduce the efficiency of the spray atomisation process in the engine. Therefore, the BTE for PODE4 became lower than PODE1 at a high engine load.

The lower BTE for DMC than the rest of the oxygenated fuels (and Jet A1) may be attributed to the lower availability of oxygen in the DMC chemical structure as species that encourages oxidation. This is because one of the main decomposition species of DMC is carbon dioxide which does not contribute to more complete combustion [1]. Consequently, the combustion with the presence of DMC may be less efficient than the rest of the oxygenated fuels.

3.3 Emission properties

Figure 6 shows the experimental and simulated residual oxygen (O_2) and nitrogen oxides (NO_x) emissions from the engine at loads of 30%, 45% and 60%. The O_2 and NO_x data are statistically significant (two-way ANOVA at a confidence level of 95%) between the engine loads only and not between the fuels, as shown in **Table 10**. This indicates that between the fuels studied, the variations in the O_2 and NO_x released in comparison to the case for Jet A1 are not sufficiently substantial to be considered as an effect of the addition of oxygenated fuels.

In Figure 6(a), the increase in engine load shows a reduction in the residual O_2 for all fuel blends. This is because a higher engine load corresponds to an increase in fuel consumption. Hence, more O_2 is required for the combustion. The demand for the O_2 is incredibly high and the additional 5% oxygen content from the oxygenated fuels is insufficient to meet the O_2 demand. This led to insignificant differences in the residual O_2 between oxygenated fuel blends and Jet A1.

In addition, the increased demand for O_2 also stems from the increased production of NO_x at increasing engine load, as shown in Figure 6(b). Generally, the emission of NO_x from engines is governed by the Zeldovich mechanism [86, 87]. Three factors have been identified to contribute to an increased NO_x production: high temperature (>1700 K), presence of oxygen and combustion time for NO_x production. For the current case, as the engine load increases, a higher amount of oxygen is required to increase the power demand. This enhances the combustion and increases the in-cylinder temperature which consequently causes more NO_x to be generated.

Figure 6 also shows the simulation results for the residual O_2 and NO_x emissions. The

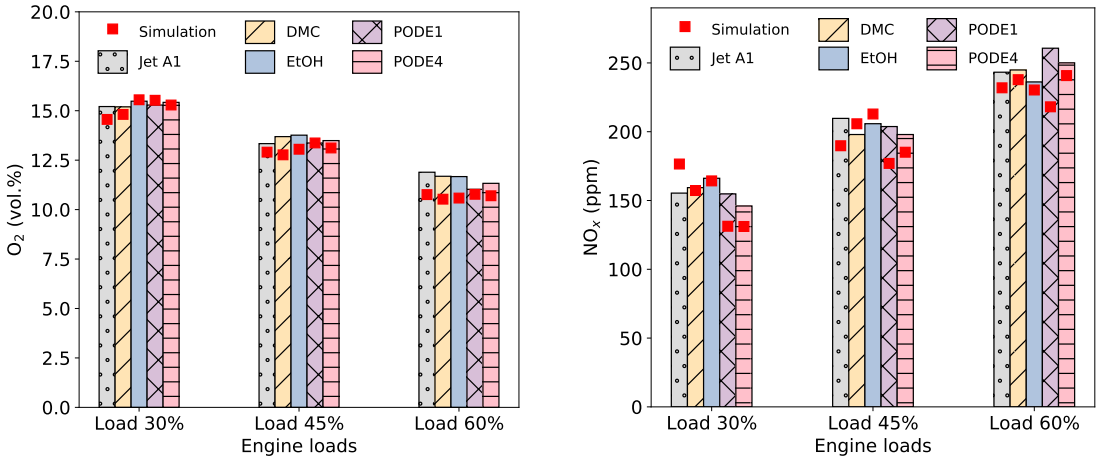

(a) Residual oxygen (O_2) emission from engine.

(b) Nitrogen oxide (NO_x) emission from engine.

Figure 6: *Experimental and simulation gaseous emission from engine at different loads for the fuel blends investigated.*

simulation results for the HC, CO_2 and CO emissions are provided in the **Section A.4** of the Supplementary material. The simulation result for O_2 is in good agreement with the experimental results but is underestimated. Meanwhile, the simulation result for NO_x emission is less agreeable with the experimental results. It can be due to the higher sensitivity of NO_x to the heat and frictional losses that are not being included in the simulation.

Figure 7 shows a clear correlation of residual oxygen emission with NO_x emission, *i.e.* increase in the emission of NO_x is accompanied by a decrease in the emission of oxygen, consistent with our previous work which explored the NO_x-O_2 relationship for different volumetric blending of PODE3 in diesel [37]. For all the engine loads, the clustering of the data point within an engine load reinforces that the effect of the oxygenated fuels on the NO_x and O_2 emission is less prominent.

The HC (unburnt hydrocarbon) emission is correlated to the combustion duration as suggested by the trend line in **Figure 8**. From the two-way ANOVA of the HC, the data is statistically significant (at confidence level of 95%) between the engine loads and the fuels, as shown in **Table 10**. For a general trend of HC with the engine load, the emission of HC decreases with the increase in engine load. The phenomenon has been discussed in detail in our previous work [37].

At an engine load of 60%, the oxygenated fuel blends release a higher concentration of HC than Jet A1, which is accompanied by a decrease in the combustion duration. This indicates that despite the oxygenated fuel blends having oxygen within their chemical structures, the reduced time for the combustion is not being compensated with the oxidative effect of the structural oxygen in the blended fuels. Hence, incomplete combustion of fuels in the engine combustion chamber occurred, followed by higher HC content for the oxygenated fuel blend [37]. Notably, despite having similar combustion duration (and same oxygen content), the HC emissions still differ among the oxygenated fuels, suggesting an effect of the molecular structure of the oxygenated fuels in the HC emissions.

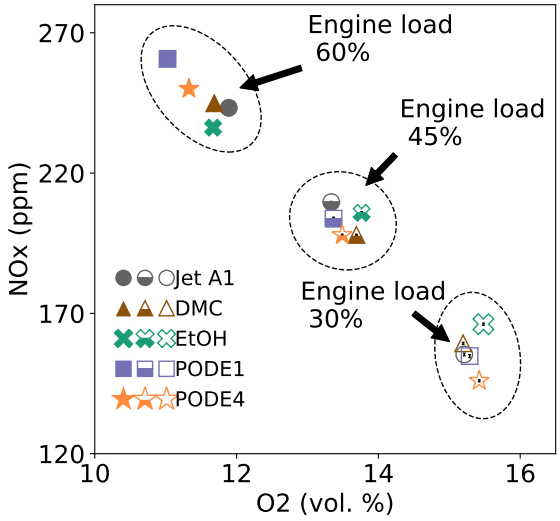

Figure 7: NO_x *emission against the residual* O_2 *emission for the engine with different fuel blends. The data shows clustering based on the engine load at 30%, 45% and 60%. The empty symbols represent the measurement at engine load of 30%; the half-filled symbols represent the measurement at engine load of 45%; while the filled symbols represent the measurement from engine load of 60%.*

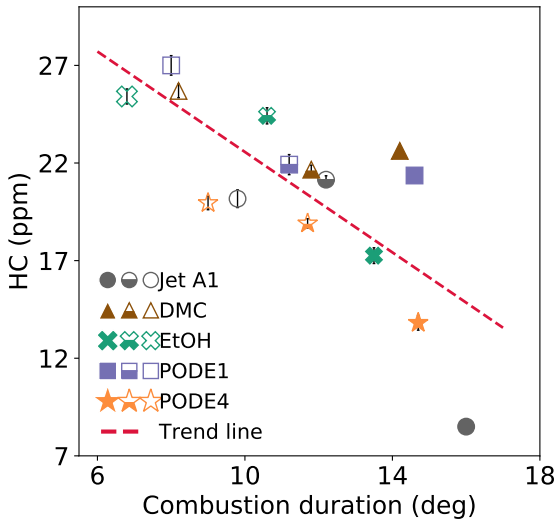

Figure 8: *The HC (unburnt hydrocarbon) emission against the combustion duration for the engine with different fuel blends. The data shows data points for engine load 30%, 45% and 60% based on the style of the symbols. The empty symbols represent engine load of 30%; the half-filled symbols represent engine load of 45%; while the filled symbols represent engine load of 60%. A trend line is plotted to guide the eye on the trend between the HC emission and the combustion duration.*

3.4 Particle size distribution

Figure 9 shows the particle size distributions (PSDs) for the fuel blends at three engine loads (30%, 45% and 60%). There is a strong reduction of the larger particles at above 10 nm (accumulation and coarse modes) for EtOH, especially at the low engine load of 30%. The reduction diminishes with the increase in the engine load up to 60%, *i.e.* the PSDs for all the oxygenated fuel blends are similar to the case for Jet A1. The rest of the oxygenated fuels have an almost negligible effect on the PSDs at all fuel engine loads. Another notable observation is an increase in smaller particles (below 10 nm, nucleation mode) for the EtOH and PODE1 fuel blend at an engine load of 30% [30]. This can be attributed to the differences in the molecular structure of the oxygenated fuels, which will be discussed in further sections.

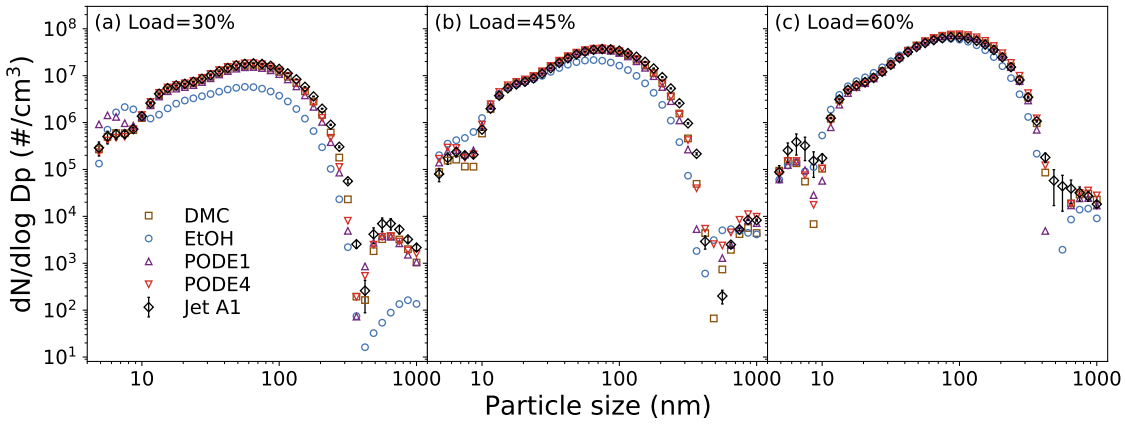

Figure 9: *Particle size distributions measured using the DMS500 at the exhaust of the engine with different fuel blends. The data in each panel are grouped by the engine load at (a) 30%, (b) 45% and 60%. The error bars show the standard error of the measurements at the exhaust over five repeats.*

3.5 Soot characterisation

In this section, the characterisation of the soot samples is critically analysed based on four techniques: Thermogravimetry analysis (TGA), Ultraviolet–visible spectroscopy (UV-Vis), Raman spectroscopy and Fourier transform infrared spectroscopy (FT-IR). ANOVA tests (summarised in **Table 11**) were performed at a confidence level of 95% for the soot properties to determine if the differences in the properties are statistically significant.

3.5.1 Oxidative properties of soot

Figure 10 shows the percentage weight and the mass change rate of the soot samples. The soot samples generally oxidise between 400 and 600 °C. In Figure 10(a), for the moderate engine load (45%), the soot from the oxygenated fuels starts to oxidise at a lower temperature than the soot from Jet A1. The ease of oxidation has a trend of PODE1

= EtOH > PODE4 > DMC > Jet A1. For the high engine load (60%), Figure 10(a), the difference narrowed except for PODE1, which also has much earlier oxidation than Jet A1. The trend changes to PODE1 > EtOH = PODE4 > DMC > Jet A1.

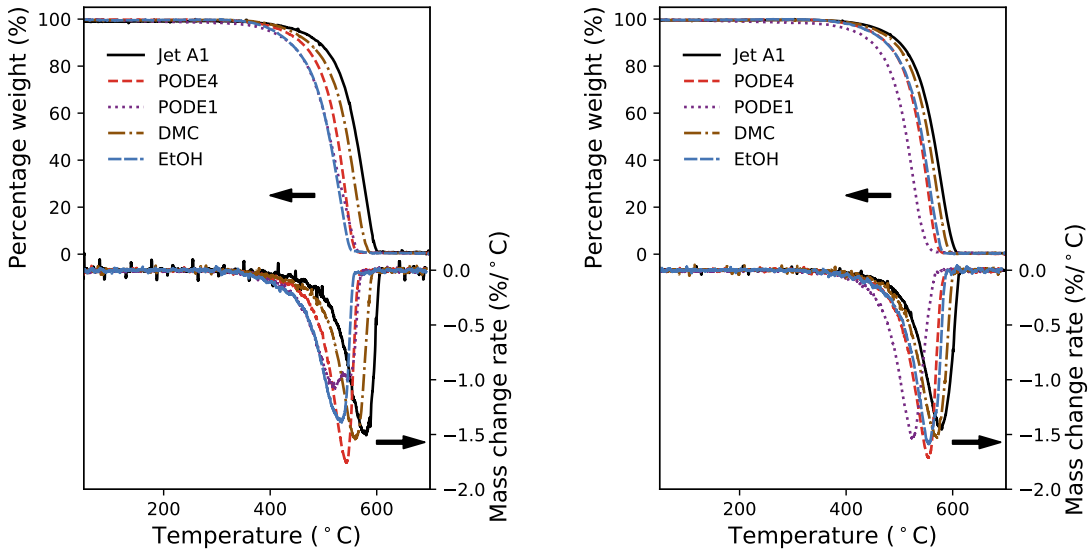

(a) Engine load 45%.

(b) Engine load 60%.

Figure 10: *Left axis: Percentage weight against the temperature of the soot samples. Right axis: The mass change rate against the temperature obtained.*

Table 6 shows the data obtained from processing the TGA profiles. The volatile organic carbon (VOC) at engine load of 45% differs among the soot samples. Jet A1 has the lowest level of VOC at 6.3%. The addition of oxygenated fuels increases the VOC content by up to 20.0% for EtOH. The rest of the soot has VOC higher than that of Jet A1. At a high engine load (60%), the soot samples from the oxygenated fuel blends are slightly higher (maximum *ca.*3%) than that of Jet A1. The trend of the VOC is consistent with the trend of the combustion duration in Figure 8. Therefore, it suggests that the higher VOC for the oxygenated fuel blends can be related to the shorter combustion duration occurring in the engine cylinder, forming more VOC rather than soot.

Two oxidation temperatures: The starting oxidation temperature (SOT) and maximum weight loss rate temperatures ($\mathrm{WLRT_{max}}$) were determined from the weight loss curve, as shown in Table 6. From Equation 2, the activation energy (E_a) of the soot oxidation under air (oxidation performance) was also computed and reported in Table 6.

The SOT and $\mathrm{WLRT_{max}}$ data were found to be statistically significant between the fuel blends. SOT and $\mathrm{WLRT_{max}}$ for the soot from all oxygenated fuel blends are lower than that of Jet A1. Notably, PODE1 has the lowest SOT and $\mathrm{WLRT_{max}}$ among the oxygenated fuels studied, *i.e.* the soot produced from PODE1 undergoes oxidation at a much lower temperature than Jet A1 and other oxygenated fuels. DMC has SOT and $\mathrm{WLRT_{max}}$ that are slightly lower than Jet A1.

The E_a data in Table 6 are statistically insignificant between the engine loads and between the fuel blends — the engine load and the oxygenated fuels have minimal impact on the

Table 6: *The percentage of volatile organic carbon (VOC), starting oxidation temperature (SOT), maximum weight loss rate temperature ($MLRT_{max}$) and the reaction activation energy (E_a) of the soot particles at engine load of 45% and 60% for different fuel blends.*

Fuel blend	Load 45%				Load 60%			
	VOC	SOT	$WLRT_{max}$	E_a	VOC	SOT	$WLRT_{max}$	E_a
Jet A1	6.3	452.1	575.6	235.7	5.4	461.0	575.8	223.5
DMC	11.4	436.9	560.0	245.5	7.6	458.8	571.8	232.5
EtOH	20.0	406.6	534.1	177.9	8.3	443.3	555.4	248.2
PODE1	12.4	398.5	523.0	141.5	8.0	411.2	524.7	209.7
PODE4	9.0	424.8	543.5	299.1	6.9	443.6	554.8	286.8

Keys:	
VOC	Volatile organic carbon (in %)
SOT	Starting oxidation temperature (in °C)
$WLRT_{max}$	Maximum weight loss rate temperatures (in °C)
E_a	Activation energy of the reaction (in kJ/mol)

soot oxidation performance. This suggests that the lower temperature (than Jet A1) for SOT and $WLRT_{max}$ cannot be attributed to the change in E_a and may be due to the differences in the properties of the soot from oxygenated fuels. This is because the reactivity of soot is found to be highly dependent on its chemical composition (surface composition), morphology and internal nanostructure [34, 53, 80]. Notably, oxygenated fuel blends produce less compactly-clustered aggregates with smaller-sized primary particles, which could be related to the production of soot with different reactivity [82]. Hence, the following subsections will attempt to investigate and explore this further.

3.5.2 The optical band gap of organic carbon and soot

Figure 11 shows the optical band gap (OBG) of organic carbon (OBG = 0.95–1.20 eV) and soot (OBG = 0.55–0.80 eV) against their average particle sizes (obtained from Section 3.4). The relationship of the OBG with the average particle size has good agreement with the size-dependency trend reported in the literature [17, 38, 44], *i.e.* the OBG decreases with the increase in the average particle size [17].

For the OBG of the organic carbon (0.95–1.20 eV), the increase in the engine load (from 45% to 60%) exhibited a decrease in the OBG. The OBG data is statistically significant across the fuels and engine loads from the calculation of the two-way ANOVA. The OBGs of the organic carbon from oxygenated fuel blends (DMC, PODE1 and PODE4) generally have lower OBGs than that of Jet A1, apart from EtOH which has a similar OBG to Jet A1. This can be related to the difference in the conjugation length of the aromatic structure of the organic carbon and functional group substitutions in the organic carbon [13]. However,

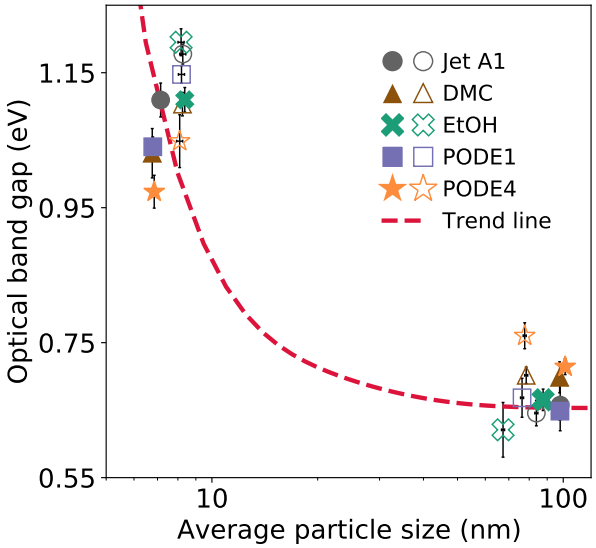

Figure 11: *Optical band gap of soot collected from engine exhaust against the average particle size. The empty symbols represent the soot collected from engine load of 45% while the filled symbols represent the soot collected from engine load of 60%. The trend line provided is to guide the eye and is based on the trend shown by Liu et al. [38] for the relationship between optical band gap against average particle size. The error bars show the standard error of the band gap measurements.*

within the same engine load, the average particle sizes are very similar among them. As calculated from the two-way ANOVA, the average particle size differences between the fuel blends are statistically insignificant. The lack of differences between the average particle size of the organic carbon suggests that the type of fuel has a lesser influence on the average particle size of organic carbon.

The differences in the OBGs of the soot (OBG = 0.55–0.80 eV) between the fuel blends and engine loads shown in Figure 11 are statistically insignificant. The OBG of the soot has less differentiation between the fuel blends because the OBG does not change much upon reaching a large average particle size [38]. The average particle size, on the other hand, is statistically significant between the engine loads and the fuel blends. Higher engine load increases the average particle size of soot. This can be due to the increased power demand for high engine load, which consumes more fuel and oxygen, coupled with the increase in the in-cylinder temperature (from more fuels combusted) favours NO_x production. These two factors promoted an increasing fuel-rich combustion condition, which causes a shift to incomplete combustion of the fuels, forming soot with larger average particle size. In addition, the average particle sizes of the soot from oxygenated fuel blends are generally smaller than that of Jet A1, likely due to the chemical effect from the oxygenated fuels and increased premixed-dominant combustion in the engine cylinder (evident from the increased ignition delay for oxygenated fuel blends).

3.5.3 Internal nanostructure of soot

Figure 12 shows the normalised Raman spectra in the region of 800—1800 cm^{-1} obtained for soot samples collected for the fuel blends at engine loads of (a) 45% and (b) 60%. Two broad, characteristic and overlapping peaks for carbonaceous materials are observed from the spectra for the soot samples, irrespective of the type of fuel blends or the engine load. Raman spectroscopy can provide information on the characteristics of the internal structure of the soot samples, *i.e.* the crystallinity and the amorphous degree of the soot. The peak at about 1345 cm^{-1} is known as the D band, attributed to the graphitic lattice breathing mode and only active in the presence of disorder or defects; the peak at about 1580 cm^{-1} is known as the G band, associated with the ideal graphitic lattice vibration mode [21, 75]. Notably, the shoulder peak at 1200 cm^{-1} is known as the D3 band, representing amorphous carbon such as organic molecules [67]. All soot samples collected from the oxygenated fuel blends have a more prominent D3 band, suggesting that the addition of oxygenated fuels promotes the incorporation of amorphous carbon to the soot nanostructure compared to the soot collected from Jet A1.

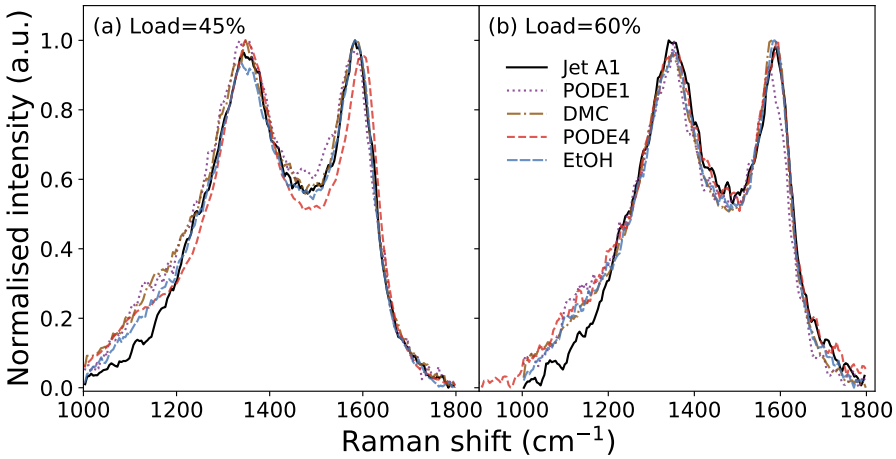

Figure 12: *Raman spectra for soot samples collected at the exhaust of the engine with different fuel blends. The data in each panel are grouped by the engine load at (a) 45% and (b) 60%.*

The soot nanostructure was analysed by calculating the intensity ratio of D1 and G (I_{D1}/I_G), which quantitatively assess the crystalline degree. A higher I_{D1}/I_G ratio indicates that the carbon layers have weaker structural order of crystalline with graphitic structure, which can result in enhanced reactivity with oxygen. The Raman spectra were fitted with four band distributions (3L1G fitting method) [63, 67]: D1, G, D3 and D4. The crystalline width (L_a) of the soot sample is then computed by a modified Knight and White [31] formula proposed by Seong and Boehman [63], as shown in **Equation 3**. In the equation, the area ratio of the D1 and G bands (A_{D1}/A_G) was used. It was established in the literature that the equation is comparable to the fringe lengths obtained by the analysis of high-resolution transmission electron microscopy images [63].

$$L_a = 4.4(A_{D1}/A_G)^{-1}. \tag{3}$$

Table 7 shows the I_{D1}/I_G and L_a data for all the samples collected at engine loads of 45% and 60%. The ANOVA results of the I_{D1}/I_G and L_a showed a significant difference between the engine loads but an insignificant one between the fuels. With the increase in the engine load, the I_{D1}/I_G and L_a decrease. The decrease in the values of I_{D1}/I_G with the increase in the engine load suggests that the lattice disorder decreases, while the L_a decrease indicates that the crystalline size of the graphitic layers also becomes smaller. This is because the engine load increases and the combustion duration is longer; hence, a more complete combustion can occur.

The variation in the I_{D1}/I_G and L_a data for the fuel blends within the same engine loads are statistically insignificant. This is consistent with the E_a results in Section 3.5.1 where the change in the soot reactivity toward oxidation is not statistically significant between the oxygenated fuels and Jet A1 as well. This suggests that the oxygenated fuels are not able to induce significant changes in graphitic lattice and crystallite width at the same load compared to Jet A1.

Table 7: *The ratio of the D1 band to G band intensity (I_{D1}/I_G) and the crystallite width (L_a) of the soot particles at engine load of 45% and 60%.*

Fuel blend	Load 45%		Load 60%	
	I_{D1}/I_G	L_a (nm)	I_{D1}/I_G	L_a (nm)
Jet A1	1.09 ± 0.02	2.25 ± 0.02	1.01 ± 0.01	1.49 ± 0.01
DMC	1.15 ± 0.01	2.54 ± 0.01	1.08 ± 0.01	2.38 ± 0.01
EtOH	1.17 ± 0.02	2.74 ± 0.04	1.02 ± 0.03	1.96 ± 0.02
PODE1	1.19 ± 0.01	2.21 ± 0.09	1.07 ± 0.03	1.78 ± 0.10
PODE4	1.17 ± 0.01	2.27 ± 0.01	1.05 ± 0.01	2.03 ± 0.09

3.5.4 Functional groups on the soot surface

Figure 13 shows the FT-IR absorbance spectra for the soot samples at different engine loads. The assignments of the peaks are based on the values reported in the literature [43, 59] for soot samples.

The spectra FT-IR absorbance spectra peaks indicate that the composition of functional groups is similar among the soot samples studied, which is consistent with the literature [20].

The soot samples FT-IR spectra exhibited the three typical sharp peaks (2962 cm^{-1}, 2926 cm^{-1} and 2858 cm^{-1}), which correspond to the aliphatic C-H stretch. There is also a weak aromatic C-H stretching peak at 3057 cm^{-1}, which is typical for structures that are highly aromatic such as graphene [46]. At 1720 cm^{-1} and 1601 cm^{-1}, the carbonyl C=O stretching peak and aromatic C=C stretching peak were observed respectively. The C-C and C-H plane deformation of aromatic groups and ether C-O-C stretching peaks appeared as a broad peak centred at 1221 cm^{-1}. Lastly, the aromatic C-H bend peak is observed at 800 cm^{-1}.

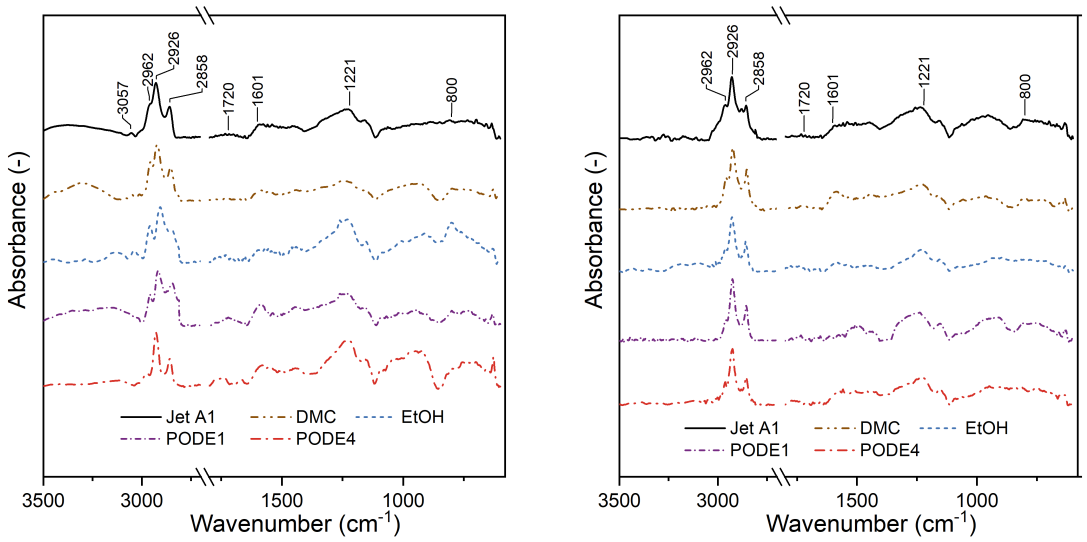

(a) Load 45%. (b) Load 60%.

Figure 13: *FT-IR absorbance spectra for soot samples from different fuel blends at engine load of (a) 45% and (b) 60%.*

A notable observation from the peak assignment can be seen from the three sharp peaks at 2962 cm^{-1}, 2926 cm^{-1} and 2858 cm^{-1} is that EtOH and PODE1 seemed to have a broader version of the three peaks. This may indicate some differences in the bonding of the methyl, methylene, and methine groups with the aromatic rings on polycyclic aromatic hydrocarbons [41, 59]. Alternatively, there can also be changed in the methylene bridges (fluorene type) maintaining the interconnection of PAHs within a network [41, 59]. In general, when comparing the signal of the peaks between soot samples from oxygenated fuel blends and Jet A1, the aliphatic C-H stretch has also a stronger signal than that of the soot from Jet A1. This suggests that the blending of oxygenated fuels in Jet A1 may increase the amount of aliphatic carbon in the soot samples.

The ratio of the C=O peak (1720 cm^{-1}) and C=C peak (1720 cm^{-1}) provides information on the relative presence of the oxygenated group $I_{1720\ cm^{-1}}/I_{1601\ cm^{-1}}$ in the soot sample. The $I_{1720\ cm^{-1}}/I_{1601\ cm^{-1}}$ ratio is often related to the soot reactivity, which can be quantified through TGA [34, 65, 66]. Additionally, the increase in oxygenated functional groups on soot may promote in allergic reactions, respiratory and cardiovascular diseases and even cancer when inhaled [47].

Table 8 shows the $I_{1720\ cm^{-1}}/I_{1601\ cm^{-1}}$ for the two engine loads investigated. The ANOVA of the $I_{1720\ cm^{-1}}/I_{1601\ cm^{-1}}$ is not significant for engine load but is significant between the fuel blends. EtOH has the highest $I_{1720\ cm^{-1}}/I_{1601\ cm^{-1}}$ ratio, double that of Jet A1. Meanwhile, DMC has the lowest $I_{1720\ cm^{-1}}/I_{1601\ cm^{-1}}$ ratio (even lower than Jet A1). PODE1 and PODE4 have a higher ratio than Jet A1 but lower than EtOH. Among PODE1 and PODE4, PODE1 has a slightly higher ratio. This is consistent with the literature where the oxygenated fuels in the fuel blends can increase the presence of oxygenated groups in soot samples [5, 58, 66].

Table 8: *The ratio of the C=O band to C=C band intensity ($I_{1720\ cm^{-1}}/I_{1601\ cm^{-1}}$) for engine load of 45% and 60%.*

Fuel blend	Load 45%	Load 60%
Jet A1	0.296	0.310
DMC	0.256	0.233
EtOH	0.601	0.645
PODE1	0.370	0.356
PODE4	0.356	0.346

3.6 Impact of oxygenated fuels on soot characteristics

In this section, the impact of the differences in the oxygenated fuel blends in affecting the resultant soot characteristics is critically discussed. Three main factors will be examined:

- Dilution effect from the oxygenated fuels,
- Combustion conditions in the engine, and
- Chemistry of the oxygenated fuels during combustion.

3.6.1 Dilution effect from the oxygenated fuels

The oxygenated fuels used in this study have different molecular structures and oxygen content. Therefore, using a fixed oxygen content in the fuel blends for different oxygenated fuels will inevitably result in different volumetric blending of each oxygenated fuels with Jet A1. The addition of oxygenated fuels could dilute the overall aromatic content of the fuel blend. The aromatic fraction of fossil fuels is thought to be one of the fuel components contributing to the increase in soot formation [10]. In the current investigation, the sequence of the volumetric blending of oxygenated fuels is given by EtOH $>$ PODE1 $>$ PODE4 $>$ DMC $>$ Jet A1. The trend in the amount of volumetric blending of the oxygenated fuels coincided with two soot properties. Among the oxygenated fuel blends, the reduction of the average particle size and the presence of oxygenated functional groups on soot has the same trend as the volumetric blending of oxygenated fuels, *i.e.* larger volumetric blending of oxygenated fuels have a greater reduction of the average particle size of soot and higher presence of oxygenated groups on soot. However, the SOT and $WLRT_{max}$ have slightly different trends than the volumetric blending. PODE1 has a lower SOT and $WLRT_{max}$ than EtOH. This shows that sole consideration of the dilution effect is insufficient in explaining the effect of oxygenated fuels on the soot characteristics.

3.6.2 Combustion conditions in the engine

The oxygenated fuel blends used in this study (with the same oxygen content) have a similar mixture LHV among the fuel blends (see Table 2). This implies that the total energy released and mean chamber temperature are similar among the oxygenated fuels studied. The HRR profiles (Figure 3) show that only EtOH has slightly higher and delayed peak HRR than the other fuel blends, which can affect the soot formation due to an increased proportion of premixed combustion for EtOH. This is more apparent by looking into the combustion duration of all fuel blends. The combustion duration trend is EtOH $<$ PODE1 $\approx$ DMC $<$ Jet A1 $\approx$ PODE4. This shows that the EtOH fuel blend has the shortest combustion phasing with a large amount of heat released (highest peak HRR in Figure 3) within a short time frame. Due to these factors, the combustion for the EtOH fuel blend is enhanced with better premixing and the duration for soot growth is reduced. This results in the formation of soot with the smallest soot average particle size and the highest VOC content (and high HC emission) for EtOH fuel blends. Despite the absence of increased premixing for DMC, PODE1 and PODE4, the trend in the average particle size of soot and the VOC content appear to be influenced by the combustion duration.

3.6.3 The chemistry of the oxygenated fuels during combustion

The impact of the chemical species from the decomposition of oxygenated fuels on soot formation is also an important factor and must be considered. The decomposition of EtOH during combustion produces hydroxyl radicals, which can promote oxidation and lead to more complete combustion [60]. This is clear from the PSD of the emission from EtOH fuel blends (see Figure 9), where the accumulation mode and coarse mode particles are significantly reduced. Additionally, the oxygenated functional groups (from FTIR) on soot collected from for EtOH blends are mainly enhanced. Interestingly, the optical band gap of the organic carbon for EtOH soot samples is similar to Jet A1 and the lowest among the oxygenated fuel blends. A decrease in the optical band gap is normally due to the presence of an oxygen-containing functional group in the aromatic structure of the samples from oxygenated fuels [13, 24]. For example, ketones can reduce the optical band gap by *ca.*0.6 eV, while the presence of the hydroxyl functional group can reduce the optical band gap by only *ca.*0.2 eV [13, 24]. This suggests that the organic carbon from the EtOH soot samples likely incorporated oxygen-containing functional groups that induce a lesser decrease in the optical band gap than the rest of the oxygenated fuels.

As for DMC, the pyrolysis and decomposition of DMC predominantly produce CO_2 directly [1, 4, 7]. Consequently, DMC forms fewer soot precursors than EtOH because it lacks carbon-carbon bonds [4, 7]. However, the production of CO_2 can result in DMC being less effective in using its embedded oxygen for soot reduction nor being incorporated into the soot structure. This is apparent from the soot characterised in the current study. The soot average particle size from the soot from DMC fuel blends is the largest among the oxygenated fuel blends. Additionally, it affected the BTE to be slightly lower than Jet A1. From the FTIR results, the composition of oxygenated species on soot is the least. This inevitably affected the SOT and $WLRT_{max}$ of the soot from DMC fuel blends to be the highest among the oxygenated fuel blends. However, the optical band gap of the

organic carbon from DMC soot is lower than EtOH. Since the composition of oxygenated species on soot is the least, the reduced optical band gap for DMC compared to EtOH may be due to the increase in the conjugation length of the aromatic structure [11] and the presence of large clustering of aromatics [3].

PODE1 and PODE4 have similar molecular structures, *i.e.* they only have carbon-oxygen-carbon bonds. It is therefore expected that similar decomposition species will be present during combustion. However, the relative amount of the decomposition species is dependent on the chain length of the PODEn. In brief, the decomposition of PODEn can produce formaldehyde and methoxy radicals [42, 77]. They are two oxygenated species that can easily convert to CO and potentially reduce their contributions to the formation of soot [68, 77, 84]. The optical band gaps of the organic carbon from the soot samples of PODE1 and PODE4 are lower than Jet A1 and EtOH. Given the similarity in the average particle sizes of the organic carbon, the relevant factor that can induce a decrease in the optical band gap is the the change in the amount of non-aromatic carbon [13, 24]. When comparing the FT-IR signal strengths at 2962 cm^{-1}, 2926 cm^{-1} and 2858 cm^{-1} of Jet A1 versus PODE1 and PODE4, the PODE1 and PODE4 soot samples have a stronger signal than that of Jet A1. It suggests that the decrease in the organic carbon optical band gap for PODE1 and PODE4 can be due to a more prominent non-aromatic carbon (aliphatic) in the PODE1 and PODE4 soot samples than in Jet A1.

The average particle sizes of soot from PODE1 and PODE4 are larger than EtOH but smaller than DMC. Similarly, their composition of oxygenated species on soot is less than EtOH but higher than DMC. This trend is consistent with the literature [83]. It can be attributed to the intermediate tendency of the oxygenated species from PODEn to participate in soot formation before being released as CO. Due to this, the oxygenated species from PODEn exhibited soot characteristics between that of DMC and EtOH. When comparing PODE1 and PODE4, soot from PODE1 has a smaller average particle size and higher composition of oxygenated species on soot than PODE4. With the oxygen content being fixed (the number of oxygenated species being fixed), it is suggested that in the current investigation, the differences between PODE1 and PODE4 are predominantly due to the dilution effect and the combustion conditions effect explained earlier.

4 Conclusions

A single-cylinder compression ignition engine was used to investigate the engine performance, gaseous emission and soot characteristics of oxygenated fuel-Jet A1 blends when combusted in the engine. Dimethyl carbonate (DMC), ethanol (EtOH), polyoxymethylene dimethyl ether 1 (PODE1) and polyoxymethylene dimethyl ether 4 (PODE4) were blended with Jet A1 at an oxygen content of 5%. Three engine loads at 30%, 45% and 60% were studied. The emissions from the engine were investigated by a gas analyser and a differential mobility spectrometer. Soot was collected from the exhaust which was further analysed with thermogravimetric analysis (TGA), Raman spectrometry, Fourier transform infrared spectroscopy (FT-IR) and ultraviolet-visible spectroscopy (UV-Vis). The data were analysed to investigate the differences in the combustion performance, gaseous emission and soot characteristics when the oxygenated fuels are blended at the

same oxygen content with Jet A1.

The addition of oxygenated fuels lengthened the ignition delay when compared to Jet A1. This results in a shorter combustion duration, which is attributed to the typically lower viscosity, lower energy density and lower cetane number (CN) of the oxygenated fuels. EtOH has the shortest combustion duration amongst the oxygenated fuels studied, contributed by the increased premixing of air and fuels before ignition, followed by PODE1, DMC and PODE4. Comparing the brake thermal efficiency (BTE) of Jet A1 and oxygenated fuel blends, the BTE for PODE4 increases by up to 4.8%, owing to the high CN of PODE4. This is followed by EtOH at 4.5% and PODE1 at 2.3%. As for DMC, the BTE is down by 2.1% from Jet A1, due to the low availability of oxygen in the DMC structure to promote oxidation.

The emission of NO_x and residual O_2 were unaffected by the type of oxygenated fuels used. Meanwhile, the emission of unburnt hydrocarbon (HC) showed dependency on the combustion duration, *i.e.* shorter combustion duration leads to higher HC emission. The particle size distribution (PSD) results showed that apart from EtOH, the addition of the oxygenated fuels has minimal effect on the PSD compared to Jet A1. Notably, the PSD of EtOH has a higher concentration of nucleation mode particles and a lower concentration of accumulation and coarse mode particles.

The TGA of the soot collected showed that the soot collected from oxygenated fuels has a lower start of oxidation temperature (SOT) than Jet A1. PODE1 has the lowest SOT and is followed by EtOH, PODE4 and DMC. Raman spectroscopy showed that the soot from oxygenated fuel blends is more amorphous than that of Jet A1, evident from the D3 band broadening on the spectra. Furthermore, the optical band gap (OBG) of the soot from UV-Vis showed that the organic carbon of the soot for PODE1, PODE4 and DMC has a smaller OBG than Jet A1; EtOH has a similar OBG as Jet A1. This is related to the types of oxygen-containing functional groups present in the organic carbon and the change in aromatic clustering that can induce changes in OBG to various extents. Lastly, the FT-IR showed an increase in the presence of oxygenated species in the soot samples for the oxygenated fuel blends, which may contribute to the reduced SOT for oxygenated fuel blend soot samples.

The differences in the soot properties have been attributed to the dilution effect, combustion conditions in the engine and the decomposition species from the oxygenated fuels during combustion. Both the reduction in average particle size of soot and the presence of oxygen-containing functional groups on soot were found to have a close relationship with the increased dilution of the aromatic fraction of Jet A1 by oxygenated fuels. In addition, the reduction in the combustion duration in the engine, induced by the oxygenated fuels, was found to decrease the average particle size of soot. Lastly, oxygenated species from the decomposition of oxygenated fuels can promote oxidation while carbon-carbon bonds from fuels may promote soot formation. This influences the soot average particle size, organic carbon OBG, SOT and even the composition of oxygenated species on soot.

Research data

Research data supporting this publication is available in the University of Cambridge data repository (doi:10.17863/CAM.89595).

Conflicts of interest

There are no conflicts to declare.

Acknowledgements

This research was supported by the National Research Foundation, Prime Minister's Office, Singapore under its Campus for Research Excellence and Technological Enterprise (CREATE) programme. A part of this study has been undertaken in the context of SimDOME project, which has received funding from the European Union's Horizon 2020 research and innovation programme under Grant Agreement number 814492. A part of this study has been undertaken in the context of OpenModel project, which has received funding from the European Union's Horizon 2020 research and innovation programme under Grant Agreement number 953167. Y. R. Tan acknowledges financial support from Fitzwilliam College Cambridge, Trinity College Cambridge and the Cambridge Trust. M. Salamanca is grateful with Universidad Nacional de Colombia-Sede Medellín for its support. M. Kraft gratefully acknowledges the support of the Alexander von Humboldt Foundation.

A Supplementary material

A.1 In-cylinder pressure simulation using different kinetic models

Three new kinetic models were created by combining the kerosene mechanism [74] with three sub-mechanisms for PODE [48], DMC [6] and EtOH [52], as detailed in Section 2.5.

The performance of the mechanisms was verified by checking if they could reproduce the experimental data from Yu et al. [85]. From the simulation result shown in **Figure 14**, it shows that the simulations results for the in-cylinder pressure remain in good agreement with the results using the original kerosene mechanism [74] when compared with the other three new kinetic models.

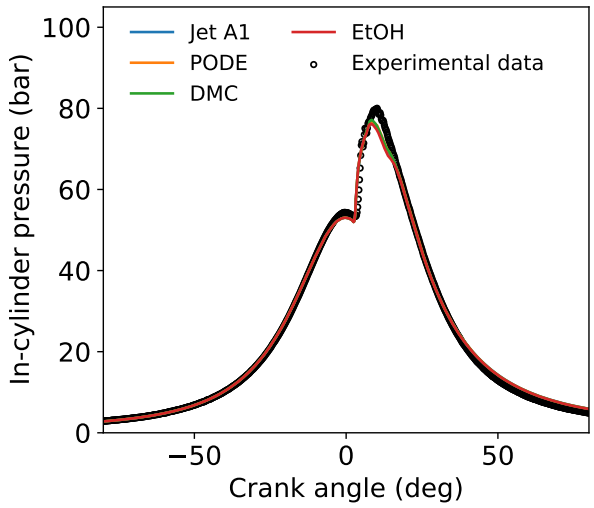

Figure 14: *Experimental in-cylinder pressure results (engine load 60%) from Yu et al. [85] and the corresponding simulation results using different kinetic mechanisms in this work.*

A.2 Calibration of in-cylinder pressure for simulation

Figure 15 shows the experimental in-cylinder pressure and the simulated in-cylinder pressure at different engine loads for Jet A1. There is a good agreement between the two in-cylinder pressures for each engine loads. Hence, it can serve as a baseline for further computation for the ignition delay, combustion duration and emission species. The same procedure of checking for good agreement between the two in-cylinder pressures for each oxygenated fuel blends have also been performed for each engine loads.

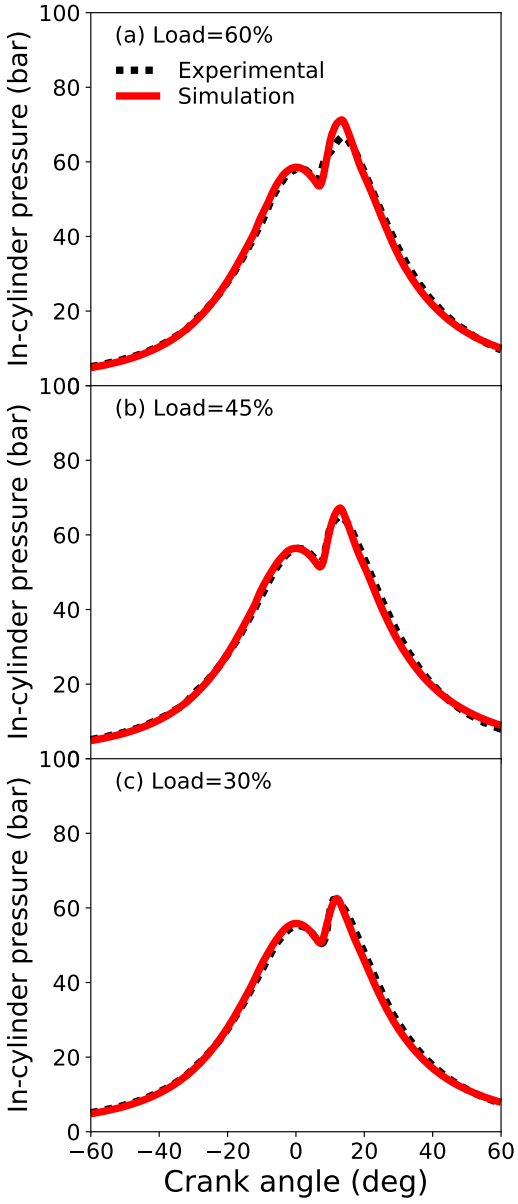

Figure 15: *Experimental and simulated in-cylinder pressure profiles for the engine with Jet A1 at engine load (a) 60%, (b) 45% and (c) 30%.*

A.3 Global sensitivity analysis

The surrogate model output generated from the High Dimensional Model Representation (HDMR) method can yield the sensitivity of each model inputs including the chemical kinetics mechanism on certain parameters. In this work, the sensitivities of five selected top five chemical reactions in the chemical mechanisms on the ignition delay and combustion duration are shown in **Figure 16**. From the two-way AVOVA, the differences in sensitivities between the fuels blends for all the chemical mechanisms are not statistically significant.

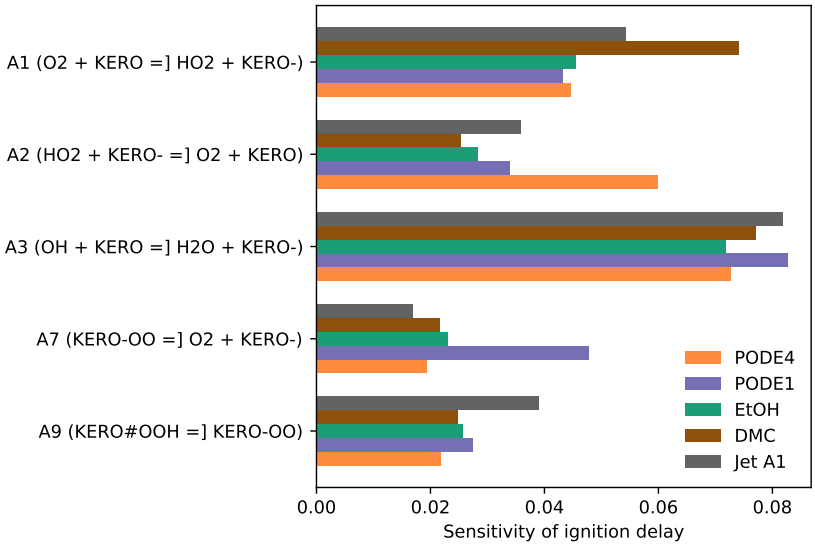

(a) Sensitivity for ignition delay.

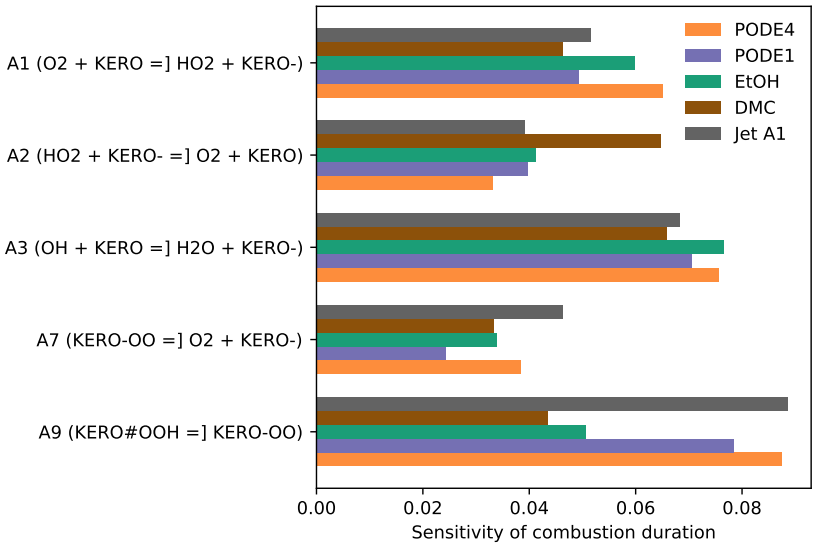

(b) Sensitivity for combustion duration.

Figure 16: *The comparison of the sensitivity of ignition delay and combustion duration for all the fuel blends investigated at engine load 60%.*

A.4 Gaseous emission from engine

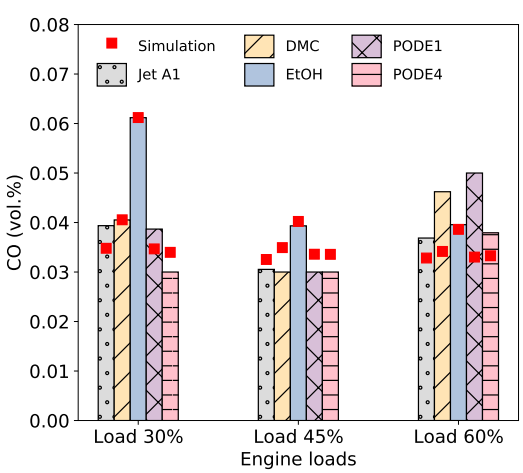

(a) Carbon monoxide emission from engine.

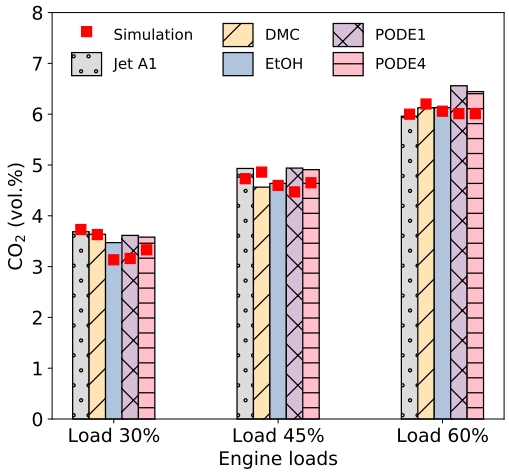

(b) Carbon dioxide emission from engine.

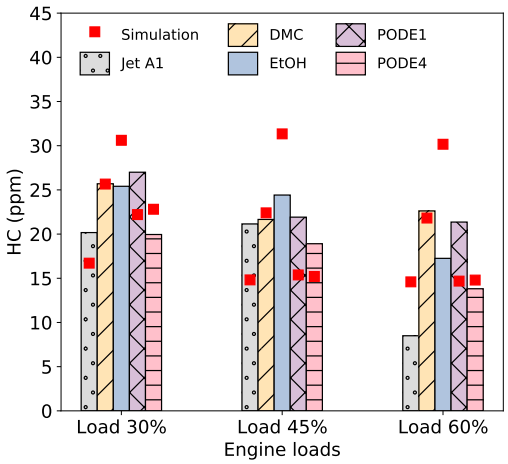

(c) Unburnt hydrocarbon emission from engine.

Figure 17: *Emission of carbon monoxide (CO), carbon dioxide (CO_2) and unburnt hydrocarbon (HC) at different engine loads, along with the simulation results.*

A.5 Analysis of variance

The analysis of variance (ANOVA) results for output terms on fuel blends (FB) and engine loads (EL) are presented in this section. ANOVA is a statistical hypothesis test where it can determine if the FB and EL are statistically significant to the output term of interest in our case. The confidence level of 95% was chosen as a suitable level of confidence for our case [78]. If the P-value is ≤ 0.05 (or the F is $>$ F crit), then the FB or EL is statistically significant.

Table 9: *The ANOVA analysis for ignition delay, combustion duration and brake thermal efficiency on the fuel blends (FB) and engine load (EL). The sensitivity analysis on the ignition delay and the combustion duration are performed on the FB and the reactions (RXN). The P-values that meet the confidence level of 95% are given a bold font.*

Output term	Source	Sum of squares	Mean square	F	P-value	F crit
ID	FB	2.21	0.55	18.9	$\mathbf{3.90 \times 10^{-4}}$	3.84
	EL	6.25	3.12	107	$\mathbf{1.72 \times 10^{-6}}$	4.46
CD	FB	10.3	2.57	22.4	$\mathbf{2.11 \times 10^{-4}}$	3.84
	EL	98.6	49.3	430	$\mathbf{7.21 \times 10^{-9}}$	4.46
BTE	FB	14.3	3.58	8.10	$\mathbf{6.47 \times 10^{-3}}$	3.84
	EL	2.45	1.22	2.77	0.122	4.46
ID	RXN	9.12×10^{-3}	2.28×10^{-3}	17.2	$\mathbf{1.20 \times 10^{-5}}$	3.01
sensitivity	FB	1.92×10^{-4}	4.81×10^{-5}	0.36	0.832	3.01
CD	RXN	5.02×10^{-3}	1.256×10^{-3}	7.62	$\mathbf{1.23 \times 10^{-3}}$	3.01
sensitivity	FB	3.47×10^{-4}	8.67×10^{-5}	0.53	0.718	3.01

Keys:

ID	Ignition delay
CD	Combustion duration
BTE	Brake thermal efficiency
RXN	Chemical reaction

Table 10: *The ANOVA analysis for oxygen (O_2), nitrogen oxide (NO_x), unburnt hydrocarbon (HC), carbon monoxide (CO) and carbon dioxide (CO_2) emission on the fuel blends (FB) and engine load (EL). The P-values that meet the confidence level of 95% are given in bold font.*

Output term	Source	Sum of squares	Mean square	F	P-value	F crit
O_2	FB	0.2778	0.0695	1.39	0.320	3.84
	EL	36.131	18.066	361	$\mathbf{1.44 \times 10^{-8}}$	4.46
NO_x	FB	114.24	28.560	0.43	0.787	3.84
	EL	20562	10281	153	$\mathbf{4.21 \times 10^{-7}}$	4.46
HC	FB	131.11	32.771	4.27	**0.039**	3.84
	EL	127.09	63.543	8.29	**0.011**	4.46
CO	FB	3.33×10^{-4}	8.33×10^{-5}	1.68	0.247	3.84
	EL	3.37×10^{-4}	1.69×10^{-4}	3.40	0.086	4.46
CO_2	FB	0.1907	0.0477	1.79	0.224	3.84
	EL	17.554	8.7768	330	$\mathbf{2.06 \times 10^{-8}}$	4.46

Table 11: *The ANOVA analysis for soot characterisation matrices on the fuel blends (FB) and engine load (EL). The P-values that meet the confidence level of 95% are given in bold font.*

Output term	Source	Sum of squares	Mean square	F	P-value	F crit
Starting oxidation	FB	3263.0	815.7	14.2	**0.012**	6.39
temperature (SOT)	EL	980.10	980.1	17.0	**0.015**	7.71
$WLRT_{max}$	FB	3215.8	804.0	21.8	$\mathbf{5.59 \times 10^{-3}}$	6.39
	EL	214.37	214.4	5.82	0.073	7.71
Activation	FB	14581	3645	3.64	0.120	6.39
energy (E_a)	EL	1020.1	1020	1.02	0.370	7.71
APS of	FB	0.919	0.230	0.96	0.515	6.39
organic carbon	EL	2.5482	2.548	10.7	**0.031**	7.71
APS of	FB	223.84	55.96	9.07	**0.028**	6.39
soot	EL	974.22	974.2	158	$\mathbf{2.31 \times 10^{-4}}$	7.71
OBG of	FB	0.0269	6.74×10^{-3}	55.3	$\mathbf{9.36 \times 10^{-4}}$	6.39
organic carbon	EL	0.0167	1.67×10^{-2}	137	$\mathbf{3.05 \times 10^{-4}}$	7.71
OBG of	FB	0.0126	3.16×10^{-3}	5.50	0.064	6.39
soot	EL	1.492×10^{-5}	1.49×10^{-5}	0.03	0.880	7.71
I_{D1}/I_G	FB	7.500×10^{-3}	1.88×10^{-3}	3.51	0.126	6.39
	EL	0.0292	2.92×10^{-2}	54.5	**0.002**	7.71
Crystalline	FB	0.4748	0.1187	2.87	0.166	6.39
width (L_a)	EL	0.56169	0.562	13.6	**0.021**	7.71
$I_{1720\ cm^{-1}}/I_{1601\ cm^{-1}}$	FB	0.16884	0.042	115	$\mathbf{2.21 \times 10^{-4}}$	6.39
	EL	1.210×10^{-5}	1.21×10^{-5}	0.03	0.865	7.71

Keys:	
$WLRT_{max}$	Maximum weight loss rate temperatures
APS	Average particle size
OBG	Optical band gap
I_{D1}/I_G	Intensity ratio of D1 and G Raman bands
$I_{1720\ cm^{-1}}/I_{1601\ cm^{-1}}$	The ratio of the C=O peak (1720 cm^{-1}) and C=C peak (1720 cm^{-1})

References

[1] A. O. G. Abdalla and D. Liu. Dimethyl carbonate as a promising oxygenated fuel for combustion: A review. *Energies*, 11(6), 2018. doi:10.3390/en11061552.

[2] M. Abián, A. D. Jensen, P. Glarborg, and M. U. Alzueta. Soot reactivity in conventional combustion and oxy-fuel combustion environments. *Energy & Fuels*, 26(8): 5337–5344, 2012. doi:10.1021/ef300670q.

[3] E. M. Adkins, J. A. Giaccai, and J. H. Miller. Computed electronic structure of polynuclear aromatic hydrocarbon agglomerates. *Proceedings of the Combustion Institute*, 36(1):957–964, 2017. doi:10.1016/j.proci.2016.06.186.

[4] L. Aguado-Deblas, J. Hidalgo-Carrillo, F. M. Bautista, C. Luna, J. Calero, A. Posadillo, A. A. Romero, D. Luna, and R. Estévez. Evaluation of dimethyl carbonate as alternative biofuel. performance and smoke emissions of a diesel engine fueled with diesel/dimethyl carbonate/straight vegetable oil triple blends. *Sustainability*, 13(4), 2021. doi:10.3390/su13041749.

[5] J. R. Agudelo, A. Álvarez, and O. Armas. Impact of crude vegetable oils on the oxidation reactivity and nanostructure of diesel particulate matter. *Combustion and Flame*, 161(11):2904–2915, 2014. doi:10.1016/j.combustflame.2014.05.013.

[6] K. Alexandrino, J. Salinas, Á. Millera, R. Bilbao, and M. U. Alzueta. Sooting propensity of dimethyl carbonate, soot reactivity and characterization. *Fuel*, 183: 64–72, 2016. doi:10.1016/j.fuel.2016.06.058.

[7] M. U. Alzueta, P. Salinas, Á. Millera, R. Bilbao, and M. Abián. A study of dimethyl carbonate conversion and its impact to minimize soot and NO emissions. *Proceedings of the Combustion Institute*, 36(3):3985–3993, 2017. doi:10.1016/j.proci.2016.07.086. URL `https://www.sciencedirect.com/science/article/pii/S1540748916303443`.

[8] B. Apicella, A. Tregrossi, A. Ciajolo, J. Abrahamson, R. Vander Wal, and C. Russo. The effect of temperature on soot properties in premixed ethylene flames. *Combustion Science and Technology*, 191(9):1558–1570, 2019. doi:10.1080/00102202.2019.1566228.

[9] T. C. Bond, S. J. Doherty, D. W. Fahey, P. M. Forster, T. Berntsen, B. J. Deangelo, M. G. Flanner, S. Ghan, B. Kärcher, D. Koch, S. Kinne, Y. Kondo, P. K. Quinn, M. C. Sarofim, M. G. Schultz, M. Schulz, C. Venkataraman, H. Zhang, S. Zhang, N. Bellouin, S. K. Guttikunda, P. K. Hopke, M. Z. Jacobson, J. W. Kaiser, Z. Klimont, U. Lohmann, J. P. Schwarz, D. Shindell, T. Storelvmo, S. G. Warren, and C. S. Zender. Bounding the role of black carbon in the climate system: A scientific assessment. *JGR: Atmospheres*, 118(11):5380–5552, 2013. doi:10.1002/jgrd.50171.

[10] M. L. Botero, S. Mosbach, J. Akroyd, and M. Kraft. Sooting tendency of surrogates for the aromatic fractions of diesel and gasoline in a wick-fed diffusion flame. *Fuel*, 153:31–39, 2015. doi:10.1016/j.fuel.2015.02.108.

[11] M. L. Botero, E. M. Adkins, S. González-Calera, H. Miller, and M. Kraft. PAH structure analysis of soot in a non-premixed flame using high-resolution transmission electron microscopy and optical band gap analysis. *Combustion and Flame*, 164:250–258, 2016. doi:10.1016/j.combustflame.2015.11.022.

[12] M. Cadrazco, A. Santamaría, and J. R. Agudelo. Chemical and nanostructural characteristics of the particulate matter produced by renewable diesel fuel in an automotive diesel engine. *Combustion and Flame*, 203:130–142, 2019. doi:10.1016/j.combustflame.2019.02.010.

[13] D. Chen and H. Wang. HOMO-LUMO energy splitting in polycyclic aromatic hydrocarbons and their derivatives. *Proceedings of the Combustion Institute*, 37(1): 953–959, 2019. doi:10.1016/j.proci.2018.06.120.

[14] H. Chen, H. Wang, Z. Chen, H. Zhao, L. Geng, N. Gao, C. Yi, and H. Xu. Research progress on the spray, combustion and emission of polyoxymethylene dimethyl ethers as a diesel blend fuel: A review. *Fuel*, 324:124731, 2022. doi:10.1016/j.fuel.2022.124731.

[15] M. Colket, J. Heyne, M. Rumizen, M. Gupta, T. Edwards, W. M. Roquemore, G. Andac, R. Boehm, J. Lovett, R. Williams, J. Condevaux, D. Turner, N. Rizk, J. Tishkoff, C. Li, J. Moder, D. Friend, and V. Sankaran. Overview of the national jet fuels combustion program. *American Institute of Aeronautics and Astronautics Journal*, 55 (4):1087–1104, 2017. doi:10.2514/1.J055361.

[16] E. Corsini, M. Marinovich, and R. Vecchi. Ultrafine particles from residential biomass combustion: A review on experimental data and toxicological response. *International Journal of Molecular Sciences*, 20(20):4992, 2019. doi:10.3390/ijms20204992.

[17] G. De Falco, G. Mattiello, M. Commodo, P. Minutolo, X. Shi, A. D'Anna, and H. Wang. Electronic band gap of flame-formed carbon nanoparticles by scanning tunneling spectroscopy. *Proceedings of the Combustion Institute*, 38(1):1805–1812, 2021. doi:10.1016/j.proci.2020.07.109.

[18] J. E. Dec. A conceptual model of DI diesel combustion based on laser-sheet imaging*. In *International Congress & Exposition*. SAE International, 1997. doi:10.4271/970873.

[19] E. F. Durand, A. P. Crayford, and M. Johnson. Experimental validation of thermophoretic and bend nanoparticle loss for a regulatory prescribed aircraft nvpm sampling system. *Aerosol Science and Technology*, 54(9):1019–1033, 2020. doi:10.1080/02786826.2020.1756212.

[20] C. Fan, J. Wei, H. Huang, M. Pan, and Z. Fu. Chemical feature of the soot emissions from a diesel engine fueled with methanol-diesel blends. *Fuel*, 297:120739, 2021. doi:10.1016/j.fuel.2021.120739.

[21] A. C. Ferrari and J. Robertson. Interpretation of Raman spectra of disordered and amorphous carbon. *Physical Review B*, 61:14095–14107, 2000. doi:10.1103/PhysRevB.61.14095.

[22] R. Fuller, P. J. Landrigan, K. Balakrishnan, G. Bathan, S. Bose-O'Reilly, M. Brauer, J. Caravanos, T. Chiles, A. Cohen, L. Corra, M. Cropper, G. Ferraro, J. Hanna, D. Hanrahan, H. Hu, D. Hunter, G. Janata, R. Kupka, B. Lanphear, M. Lichtveld, K. Martin, A. Mustapha, E. Sanchez-Triana, K. Sandilya, L. Schaefli, J. Shaw, J. Seddon, W. Suk, M. M. Téllez-Rojo, and C. Yan. Pollution and health: a progress update. *The Lancet Planetary Health*, 1(1):1–13, 2022. doi:10.1016/S2542-5196(22)00090-0.

[23] M. A. Ghadikolaei, P. K. Wong, C. S. Cheung, Z. Ning, K.-F. Yung, J. Zhao, N. K. Gali, and A. V. Berenjestanaki. Impact of lower and higher alcohols on the physicochemical properties of particulate matter from diesel engines: A review. *Renewable and Sustainable Energy Reviews*, 143:110970, 2021. doi:10.1016/j.rser.2021.110970.

[24] J. A. Giaccai and J. H. Miller. Examination of the electronic structure of oxygen-containing PAH dimers and trimers. *Proceedings of the Combustion Institute*, 37(1): 903–910, 2019. doi:10.1016/j.proci.2018.05.057.

[25] E. Hegnsholt, M. Holm, P. Herhold, A. de Mur, and J. Burchardt. The road ahead for low-carbon fuels, 2022. URL https://www.bcg.com/publications/2022/the-road-ahead-for-low-carbon-fuels. Last accessed 8 May 2022.

[26] J. B. Heywood. *Internal Combustion Engine Fundamentals*, volume 10: Combustion in Compression-Ignition Engines. McGraw-Hill Education, New York, 2nd edition, 2018.

[27] Y. Hua, F. Liu, H. Wu, C.-F. Lee, and Y. Li. Effects of alcohol addition to traditional fuels on soot formation: A review. *International Journal of Engine Research*, 22(5): 1395–1420, 2021. doi:10.1177/1468087420910886.

[28] International Energy Agency. World Energy Outlook, 2021. URL https://www.iea.org/reports/world-energy-outlook-2021. Last accessed 8 May 2022.

[29] I. C. Jaramillo, A. Sturrock, H. Ghiassi, D. J. Woller, C. E. Deering-Rice, J. S. Lighty, R. Paine, C. Reilly, and K. E. Kelly. Effects of fuel components and combustion particle physicochemical properties on toxicological responses of lung cells. *Journal of Environmental Science and Health, Part A*, 53(4):295–309, 2018. doi:10.1080/10934529.2017.1400793.

[30] D. B. Kittelson. Engines and nanoparticles: a review. *Journal of Aerosol Science*, 29(5):575–588, 1998. doi:10.1016/S0021-8502(97)10037-4.

[31] D. S. Knight and W. B. White. Characterization of diamond films by Raman spectroscopy. *Journal of Materials Research*, 4(2):385–393, 1989. doi:10.1557/JMR.1989.0385.

[32] K. Kohse-Höinghaus, P. Oβwald, T. A. Cool, T. Kasper, N. Hansen, F. Qi, C. K. Westbrook, and P. R. Westmoreland. Biofuel combustion chemistry: From ethanol to biodiesel. *Angewandte Chemie International Edition*, 49(21):3572–3597, 2010. doi:10.1002/anie.200905335.

[33] J. Lai, K. F. Lee, J. H. Yap, B. Yadollahi, A. Bhave, Z. Zhang, X. Ma, and H. Xu. Effects of ethanol-blended fuel on combustion characteristics, gaseous and particulate emissions in gasoline direct injection (GDI) engines. *Symposium on International Automotive Technology, SAE International*, 2021. doi:10.4271/2021-26-0356.

[34] M. Lapuerta, J. Rodríguez–Fernández, and J. Sánchez-Valdepeñas. Soot reactivity analysis and implications on diesel filter regeneration. *Progress in Energy and Combustion Science*, 78:100833, 2020. doi:10.1016/j.pecs.2020.100833.

[35] D. S. Lee, D. W. Fahey, A. Skowron, M. R. Allen, U. Burkhardt, Q. Chen, S. J. Doherty, S. Freeman, P. M. Forster, J. Fuglestvedt, A. Gettelman, R. De León, L. L. Lim, M. Lund, R. Millar, B. Owen, J. E. Penner, G. Pitari, M. Prather, R. Sausen, and L. J. Wilcox. The contribution of global aviation to anthropogenic climate forcing for 2000 to 2018. *Atmospheric Environment*, 244:117834, 2021. doi:10.1016/j.atmosenv.2020.117834.

[36] Q. Lin, K. L. Tay, W. Yu, W. Yang, and Z. Wang. Effects of polyoxymethylene dimethyl ether 3 (PODE3) addition and injection pressure on combustion performance and particle size distributions in a diesel engine. *Fuel*, 283:119347, 2021. doi:10.1016/j.fuel.2020.119347.

[37] Q. Lin, K. L. Tay, W. Yu, Y. Zong, W. Yang, L.-H. Rivellini, M. Ma, and A. K. Y. Lee. Polyoxymethylene dimethyl ether 3 (PODE3) as an alternative fuel to reduce aerosol pollution. *Journal of Cleaner Production*, 285:124857, 2021. doi:10.1016/j.jclepro.2020.124857.

[38] C. Liu, A. V. Singh, C. Saggese, Q. Tang, D. Chen, K. Wan, M. Vinciguerra, M. Commodo, G. De Falco, P. Minutolo, A. D'Anna, and H. Wang. Flame-formed carbon nanoparticles exhibit quantum dot behaviors. *Proceedings of the National Academy of Sciences*, 116(26):12692–12697, 2019. doi:10.1073/pnas.1900205116.

[39] H. Liu, Z. Wang, Y. Li, Y. Zheng, T. He, and J. Wang. Recent progress in the application in compression ignition engines and the synthesis technologies of polyoxymethylene dimethyl ethers. *Applied Energy*, 233-234:599–611, 2019. doi:10.1016/j.apenergy.2018.10.064.

[40] J. Liu, L. Wang, P. Wang, P. Sun, H. Liu, Z. Meng, L. Zhang, and H. Ma. An overview of polyoxymethylene dimethyl ethers as alternative fuel for compression ignition engines. *Fuel*, 318:123582, 2022. doi:10.1016/j.fuel.2022.123582.

[41] Y. Liu, C. Song, G. Lv, X. Wang, and N. Li. Virgin and extracted soots in premixed methane flames: A comparison of surface functional groups, graphitization degree, and oxidation reactivity. *Energy & Fuels*, 31(6):6413–6421, 2017. doi:10.1021/acs.energyfuels.6b03011.

[42] L. Marrodán, F. Monge, Á. Millera, R. Bilbao, and M. U. Alzueta. Dimethoxymethane oxidation in a flow reactor. *Combustion Science and Technology*, 188(4-5):719–729, 2016. doi:10.1080/00102202.2016.1138826.

[43] J. T. Mckinnon, E. Meyer, and J. B. Howard. Infrared analysis of flame-generated PAH samples. *Combustion and Flame*, 105(1):161–166, 1996. doi:10.1016/0010-2180(95)00185-9.

[44] A. Menon, J. A. H. Dreyer, J. W. Martin, J. Akroyd, J. Robertson, and M. Kraft. Optical band gap of cross-linked, curved, and radical polyaromatic hydrocarbons. *Physical Chemistry Chemical Physics*, 21:16240–16251, 2019. doi:10.1039/C9CP02363A.

[45] K. Mu, I. Kharisov, C. Follette, A. Gordon, N. Boutin, and R. Whalen. What it will take to reap the rewards of renewable fuels, 2022. URL https://www.bcg.com/publications/2022/what-it-will-take-to-reap-the-rewards-of-renewable-fuels. Last accessed 8 May 2022.

[46] M. Naebe, J. Wang, A. Amini, H. Khayyam, N. Hameed, L. H. Li, Y. Chen, and B. Fox. Mechanical property and structure of covalent functionalised graphene/epoxy nanocomposites. *Scientific Reports*, 4:4375, 2014. doi:10.1038/srep04375.

[47] R. Niessner. The many faces of soot: Characterization of soot nanoparticles produced by engines. *Angewandte Chemie International Edition*, 53(46):12366–12379, 2014. doi:10.1002/anie.201402812.

[48] B. Niu, M. Jia, Y. Chang, H. Duan, X. Dong, and P. Wang. Construction of reduced oxidation mechanisms of polyoxymethylene dimethyl ethers (PODE1–6) with consistent structure using decoupling methodology and reaction rate rule. *Combustion and Flame*, 232:111534, 2021. doi:10.1016/j.combustflame.2021.111534.

[49] U. D. of Energy. Alternative fuels data center for ethanol, 2022. URL https://afdc.energy.gov/fuels/ethanol.html. Last accessed 28 June 2022.

[50] V. Page, J. Lai, O. Parry, S. Mosbach, and A. Bhave. Evaluating emissions in a modern compression ignition engine using multi-dimensional PDF-based stochastic simulations and statistical surrogate generation. In *International Powertrains, Fuels & Lubricants Meeting*. SAE International, 2018. doi:10.4271/2018-01-1739.

[51] M. Pan, W. Qian, Y. Wang, C. Wu, and H. Huang. Effect of dimethoxymethane (DMM) additive on combustion and emission characteristics under different working conditions in CI engines. *Fuel*, 284:119304, 2021. doi:10.1016/j.fuel.2020.119304.

[52] W. Pejpichestakul, E. Ranzi, M. Pelucchi, A. Frassoldati, A. Cuoci, A. Parente, and T. Faravelli. Examination of a soot model in premixed laminar flames at fuel-rich conditions. *Proceedings of the Combustion Institute*, 37(1):1013–1021, 2019. doi:10.1016/j.proci.2018.06.104.

[53] S. Rana, M. Saxena, and R. Maurya. A review on morphology, nanostructure, chemical composition, and number concentration of diesel particulate emissions. *Environmental Science and Pollution Research*, 29:15432–15489, 2022. doi:10.1007/s11356-021-15999-5.

[54] J. Rodríguez-Fernández, F. Oliva, and R. A. Vázquez. Characterization of the diesel soot oxidation process through an optimized thermogravimetric method. *Energy & Fuels*, 25(5):2039–2048, 2011. doi:10.1021/ef200194m.

[55] C. Russo, M. Alfè, J.-N. Rouzaud, F. Stanzione, A. Tregrossi, and A. Ciajolo. Probing structures of soot formed in premixed flames of methane, ethylene and benzene. *Proceedings of the Combustion Institute*, 34(1):1885–1892, 2013. doi:10.1016/j.proci.2012.06.127.

[56] C. Russo, B. Apicella, J. Lighty, A. Ciajolo, and A. Tregrossi. Optical properties of organic carbon and soot produced in an inverse diffusion flame. *Carbon*, 124: 372–379, 2017. doi:10.1016/j.carbon.2017.08.073.

[57] C. Russo, B. Apicella, A. Tregrossi, A. Ciajolo, K. C. Le, S. Török, and P.-E. Bengtsson. Optical band gap analysis of soot and organic carbon in premixed ethylene flames: Comparison of in-situ and ex-situ absorption measurements. *Carbon*, 158: 89–96, 2020. doi:10.1016/j.carbon.2019.11.087.

[58] M. Salamanca, F. Mondragón, J. R. Agudelo, and A. Santamaría. Influence of palm oil biodiesel on the chemical and morphological characteristics of particulate matter emitted by a diesel engine. *Atmospheric Environment*, 62:220–227, 2012. doi:10.1016/j.atmosenv.2012.08.031.

[59] A. Santamaría, F. Mondragón, A. Molina, N. D. Marsh, E. G. Eddings, and A. F. Sarofim. FT-IR and 1H NMR characterization of the products of an ethylene inverse diffusion flame. *Combustion and Flame*, 146(1):52–62, 2006. doi:10.1016/j.combustflame.2006.04.008.

[60] S. M. Sarathy, P. Oβwald, N. Hansen, and K. Kohse-Höinghaus. Alcohol combustion chemistry. *Progress in Energy and Combustion Science*, 44:40–102, 2014. doi:10.1016/j.pecs.2014.04.003.

[61] D. E. Schraufnagel. The health effects of ultrafine particles. *Experimental & Molecular Medicine*, 52:311–317, 2020. doi:10.1038/s12276-020-0403-3.

[62] T. Schripp, B. E. Anderson, U. Bauder, B. Rauch, J. C. Corbin, G. J. Smallwood, P. Lobo, E. C. Crosbie, M. A. Shook, R. C. Miake-Lye, Z. Yu, A. Freedman, P. D. Whitefield, C. E. Robinson, S. L. Achterberg, M. Köhler, P. Oβwald, T. Grein, D. Sauer, C. Voigt, H. Schlager, and P. LeClercq. Aircraft engine particulate matter emissions from sustainable aviation fuels: Results from ground-based measurements during the NASA/DLR campaign ECLIF2/ND-MAX. *Fuel*, 325:124764, 2022. doi:10.1016/j.fuel.2022.124764.

[63] H. J. Seong and A. L. Boehman. Evaluation of Raman parameters using visible Raman microscopy for soot oxidative reactivity. *Energy & Fuels*, 27(3):1613–1624, 2013. doi:10.1021/ef301520y.

[64] A. Smallbone, A. Bhave, and P. Man. High-dimensional sensitivity analysis applied at vehicle component and system level in the context of CO_2 exhaust emissions. In *SAE 2014 International Powertrain, Fuels & Lubricants Meeting*. SAE International, 2014. doi:10.4271/2014-01-2564.

[65] J. Song, M. Alam, and A. L. Boehman. Impact of alternative fuels on soot properties and DPF regeneration. *Combustion Science and Technology*, 179(9):1991–2037, 2007. doi:10.1080/00102200701386099.

[66] J. A. Soriano, J. R. Agudelo, A. F. López, and O. Armas. Oxidation reactivity and nanostructural characterization of the soot coming from farnesane - a novel diesel fuel derived from sugar cane. *Carbon*, 125:516–529, 2017. doi:10.1016/j.carbon.2017.09.090.

[67] C. Sun, J. Martin, and A. L. Boehman. Impacts of advanced diesel combustion operation and fuel formulation on soot nanostructure and reactivity. *Fuel*, 276:118080, 2020. doi:10.1016/j.fuel.2020.118080.

[68] W. Sun, G. Wang, S. Li, R. Zhang, B. Yang, J. Yang, Y. Li, C. K. Westbrook, and C. K. Law. Speciation and the laminar burning velocities of poly(oxymethylene) dimethyl ether 3 (POMDME3) flames: An experimental and modeling study. *Proceedings of Combustion Institute*, 36(1):1269–1278, 2017. doi:10.1016/j.proci.2016.05.058.

[69] Y. R. Tan, M. L. Botero, Y. Sheng, J. A. H. Dreyer, R. Xu, W. Yang, and M. Kraft. Sooting characteristics of polyoxymethylene dimethyl ether blends with diesel in a diffusion flame. *Fuel*, 224:499–506, 2018. doi:10.1016/j.fuel.2018.03.051.

[70] Y. R. Tan, M. Salamanca, J. Akroyd, and M. Kraft. How do the oxygenated functional groups in ether, carbonate and alcohol affect soot formation in Jet A2 diffusion flames? *Combustion and Flame*, page 111849, 2021. doi:10.1016/j.combustflame.2021.111849.

[71] Y. R. Tan, M. Salamanca, J. Bai, J. Akroyd, and M. Kraft. Structural effects of C3 oxygenated fuels on soot formation in ethylene coflow diffusion flames. *Combustion and Flame*, 232:111512, 2021. doi:10.1016/j.combustflame.2021.111512.

[72] Y. R. Tan, M. Salamanca, L. Pascazio, J. Akroyd, and M. Kraft. The effect of poly(oxymethylene) dimethyl ethers ($PODE_3$) on soot formation in ethylene/$PODE_3$ laminar coflow diffusion flames. *Fuel*, 283:118769, 2021. doi:10.1016/j.fuel.2020.118769.

[73] J. Tauc, R. Grigorovici, and A. Vancu. Optical properties and electronic structure of amorphous germanium. *Physica Status Solidi (B)*, 15(2):627–637, 1966. doi:10.1002/pssb.19660150224.

[74] K. L. Tay, W. Yang, J. Li, D. Zhou, W. Yu, F. Zhao, S. K. Chou, and B. Mohan. Numerical investigation on the combustion and emissions of a kerosene-diesel fueled compression ignition engine assisted by ammonia fumigation. *Applied Energy*, 204: 1476–1488, 2017. doi:10.1016/j.apenergy.2017.03.100.

[75] F. Tuinstra and J. L. Koenig. Raman spectrum of graphite. *The Journal of Chemical Physics*, 53(3):1126–1130, 1970. doi:10.1063/1.1674108.

[76] P. Verma, M. Jafari, S. Ashrafur Rahman, E. Pickering, S. Stevanovic, A. Dowell, R. Brown, and Z. Ristovski. The impact of chemical composition of oxygenated fuels on morphology and nanostructure of soot particles. *Fuel*, 259:116167, 2020. doi:10.1016/j.fuel.2019.116167.

[77] F. H. Vermeire, H.-H. Carstensen, O. Herbinet, F. Battin-Leclerc, G. B. Marin, and K. M. Van Geem. Experimental and modeling study of the pyrolysis and combustion of dimethoxymethane. *Combustion and Flame*, 190:270–283, 2018. doi:10.1016/j.combustflame.2017.12.001.

[78] I. Veza, A. Deniz Karaoglan, E. Ileri, A. Afzal, A. Tuan Hoang, N. Tamaldin, S. Gazali Herawan, M. M. Abbas, and M. Farid Muhamad Said. Multi-objective optimization of diesel engine performance and emission using grasshopper optimization algorithm. *Fuel*, 323:124303, 2022. doi:10.1016/j.fuel.2022.124303.

[79] Y. Wang, M. Pan, H. Huang, X. Zhou, J. Wei, and H. Chen. Physicochemical properties of exhaust soot from lower and higher alcohols: Characterizations and impact on soot oxidation behavior. *Fuel*, 311:122524, 2022. doi:https://doi.org/10.1016/j.fuel.2021.122524.

[80] J. Wei and Y. Wang. Effects of biodiesels on the physicochemical properties and oxidative reactivity of diesel particulates: A review. *Science of The Total Environment*, 788:147753, 2021. doi:10.1016/j.scitotenv.2021.147753.

[81] J. Wei, W. Lu, M. Pan, Y. Liu, X. Cheng, and C. Wang. Physical properties of exhaust soot from dimethyl carbonate-diesel blends: Characterizations and impact on soot oxidation behavior. *Fuel*, 279:118441, 2020. doi:10.1016/j.fuel.2020.118441.

[82] J. Wei, Y. Zeng, M. Pan, Y. Zhuang, L. Qiu, T. Zhou, and Y. Liu. Morphology analysis of soot particles from a modern diesel engine fueled with different types of oxygenated fuels. *Fuel*, 267:117248, 2020. doi:10.1016/j.fuel.2020.117248.

[83] J. Wei, W. Lu, Y. Zeng, H. Huang, M. Pan, and Y. Liu. Physicochemical properties and oxidation reactivity of exhaust soot from a modern diesel engine: Effect of oxyfuel type. *Combustion and Flame*, 238:111940, 2022. doi:10.1016/j.combustflame.2021.111940.

[84] F. Yan, L. Xu, Y. Wang, S. Park, S. M. Sarathy, and S. H. Chung. On the opposing effects of methanol and ethanol addition on PAH and soot formation in ethylene counterflow diffusion flames. *Combustion and Flame*, 202:228–242, 2019. doi:10.1016/j.combustflame.2019.01.020.

[85] W. Yu, Y. Zong, Q. Lin, K. Tay, F. Zhao, W. Yang, and M. Kraft. Experimental study on engine combustion and particle size distributions fueled with Jet A-1. *Fuel*, 263: 116747, 2020. doi:10.1016/j.fuel.2019.116747.

[86] I. Yusri, R. Mamat, M. Akasyah, M. Jamlos, and A. Yusop. Evaluation of engine combustion and exhaust emissions characteristics using diesel/butanol blended fuel. *Applied Thermal Engineering*, 156:209–219, 2019. doi:10.1016/j.applthermaleng.2019.02.028.

[87] Y. Zeldovich. The oxidation of nitrogen on combustion and explosions. *Acta Physiochimica U.S.S.R.*, 21:577–628, 1946. doi:10.1515/9781400862979.364.

[88] Q. Zhu, Y. Zong, W. Yu, W. Yang, and M. Kraft. Understanding the blending effect of polyoxymethylene dimethyl ethers as additive in a common-rail diesel engine. *Applied Energy*, 300:117380, 2021. doi:10.1016/j.apenergy.2021.117380.

[89] Q. Zhu, Y. Zong, W. Yu, W. Yang, and M. Kraft. Understanding the particulate formation process in the engine fuelled with diesel/Jet A-1 blends. *Fuel*, 313:122675, 2022. doi:10.1016/j.fuel.2021.122675.